Molecular Therapy
Original Article

Preventing occludin tight-junction disruption via inhibition of microRNA-193b-5p attenuates viral load and influenza-induced lung injury

Chirag M. Vaswani,[1,2] Amir K. Varkouhi,[3] Sahil Gupta,[2,4,5] Amin M. Ektesabi,[2,4] James N. Tsoporis,[2] Sadiya Yousef,[2] Pamela J. Plant,[2] Adriana L. da Silva,[6,7] Yuchen Cen,[8] Yi-Chieh Tseng,[8] Sabrina S. Batah,[9] Alexandre T. Fabro,[9] Suzanne L. Advani,[2] Andrew Advani,[2] Howard Leong-Poi,[2,4] John C. Marshall,[2,4] Cristiana C. Garcia,[10,11] Patricia R.M. Rocco,[6,7] Guillermo M. Albaiceta,[12,13,14] Steffen Sebastian-Bolz,[1] Tania H. Watts,[15] Theo J. Moraes,[8,16] Vera L. Capelozzi,[18] and Claudia.C. dos Santos[1,2,4,17,19]

[1]Department of Physiology, Temerty Faculty of Medicine, University of Toronto, Toronto, ON, Canada; [2]Keenan Research Centre for Biomedical Science, St. Michael's Hospital, Toronto, ON, Canada; [3]Department of Chemistry and Environmental Science, New Jersey Institute of Technology, Newark, NJ, USA; [4]Institute of Medical Sciences, Faculty of Medicine, University of Toronto, Toronto, ON, Canada; [5]Faculty of Medicine, School of Medicine, The University of Queensland, Herston, QLD 4006, Australia; [6]Laboratory of Pulmonary Investigation, Carlos Chagas Filho Institute of Biophysics, Federal University of Rio de Janeiro, Rio de Janeiro, Brazil; [7]COVID-19 Virus Network from Ministry of Science, Technology, and Innovation, Brazilian Council for Scientific and Technological Development, and Foundation Carlos Chagas Filho Research Support of the State of Rio de Janeiro, Brazil; [8]Program in Translational Medicine, SickKids Research Institute, Toronto, ON, Canada; [9]Department of Pathology and Legal Medicine, Ribeirão Preto Medical School, University of São Paulo, São Paulo, Brazil; [10]Laboratory of Respiratory, Exanthematic Viruses, Enterovirus and Viral Emergencies, Oswaldo Cruz Institute, FIOCRUZ, Rio de Janeiro, Brazil; [11]Integrated Research Group on Biomarkers. René Rachou Institute, FIOCRUZ Minas, Belo Horizonte, Brazil; [12]Departamento de Biología Funcional, Instituto Universitario de Oncología del Principado de Asturias, Universidad de Oviedo, Oviedo, Spain; [13]Unidad de Cuidados Intensivos Cardiológicos, Hospital Universitario Central de Asturias, Oviedo, Spain; [14]CIBER-Enfermedades Respiratorias, Instituto de Salud Carlos III, Madrid, Spain; [15]Department of Immunology, Temerty Faculty of Medicine, University of Toronto, Toronto, ON, Canada; [16]Department of Pediatrics University of Toronto and Respirology, Hospital for Sick Children, Toronto, ON, Canada; [17]Laboratory Medicine and Pathobiology, Faculty of Medicine, University of Toronto, Toronto, ON, Canada; [18]Department of Pathology, University of São Paulo, São Paulo, Brazil; [19]Interdepartmental Division of Critical Care, St Michael's Hospital, University of Toronto, Toronto, ON, Canada

Virus-induced lung injury is associated with loss of pulmonary epithelial-endothelial tight junction integrity. While the alveolar-capillary membrane may be an indirect target of injury, viruses may interact directly and/or indirectly with miRs to augment their replication potential and evade the host antiviral defense system. Here, we expose how the influenza virus (H1N1) capitalizes on host-derived interferon-induced, microRNA (miR)-193b-5p to target occludin and compromise antiviral defenses. Lung biopsies from patients infected with H1N1 revealed increased miR-193b-5p levels, marked reduction in occludin protein, and disruption of the alveolar-capillary barrier. In C57BL/6 mice, the expression of miR-193b-5p increased, and occludin decreased, 5–6 days post-infection with influenza (PR8). Inhibition of miR-193b-5p in primary human bronchial, pulmonary microvascular, and nasal epithelial cells enhanced antiviral responses. miR-193b-deficient mice were resistant to PR8. Knockdown of occludin, both *in vitro* and *in vivo*, and overexpression of miR-193b-5p reconstituted susceptibility to viral infection. miR-193b-5p inhibitor mitigated loss of occludin, improved viral clearance, reduced lung edema, and augmented survival in infected mice. Our results elucidate how the innate immune system may be exploited by the influenza virus and how strategies that prevent loss of occludin and preserve tight junction function may limit susceptibility to virus-induced lung injury.

INTRODUCTION

Inadequate immunity to the continually evolving influenza virus (IV) variants cause sporadic outbreaks that are often difficult to predict and continue to remain a public health concern.[1] The 1918 pandemic claimed the lives of over 40 million people.[2] The 2009 H1N1 pandemic strain resulted in an estimated 500,000 fatalities.[3] IV can reach deep into the lung airspaces and cause alveolar-capillary injury, diffuse alveolar damage, exudative edema, and immune cell infiltration resulting in acute respiratory distress syndrome (ARDS)[4,5]; the leading cause of multi-organ failure[4,6] and mortality in critically ill influenza-infected patients.[7]

Received 2 March 2023; accepted 14 June 2023;
https://doi.org/10.1016/j.ymthe.2023.06.011.

Correspondence: Claudia. C. dos Santos, MSc, MD, Clinician-Scientist, Associate Professor of Medicine, Interdepartmental Division of Critical Care, St. Michael's Hospital/University of Toronto, 30 Bond Street, Room 4-008, Toronto, ON M5B 1WB, Canada.
E-mail: claudia.dossantos@unityhealth.to

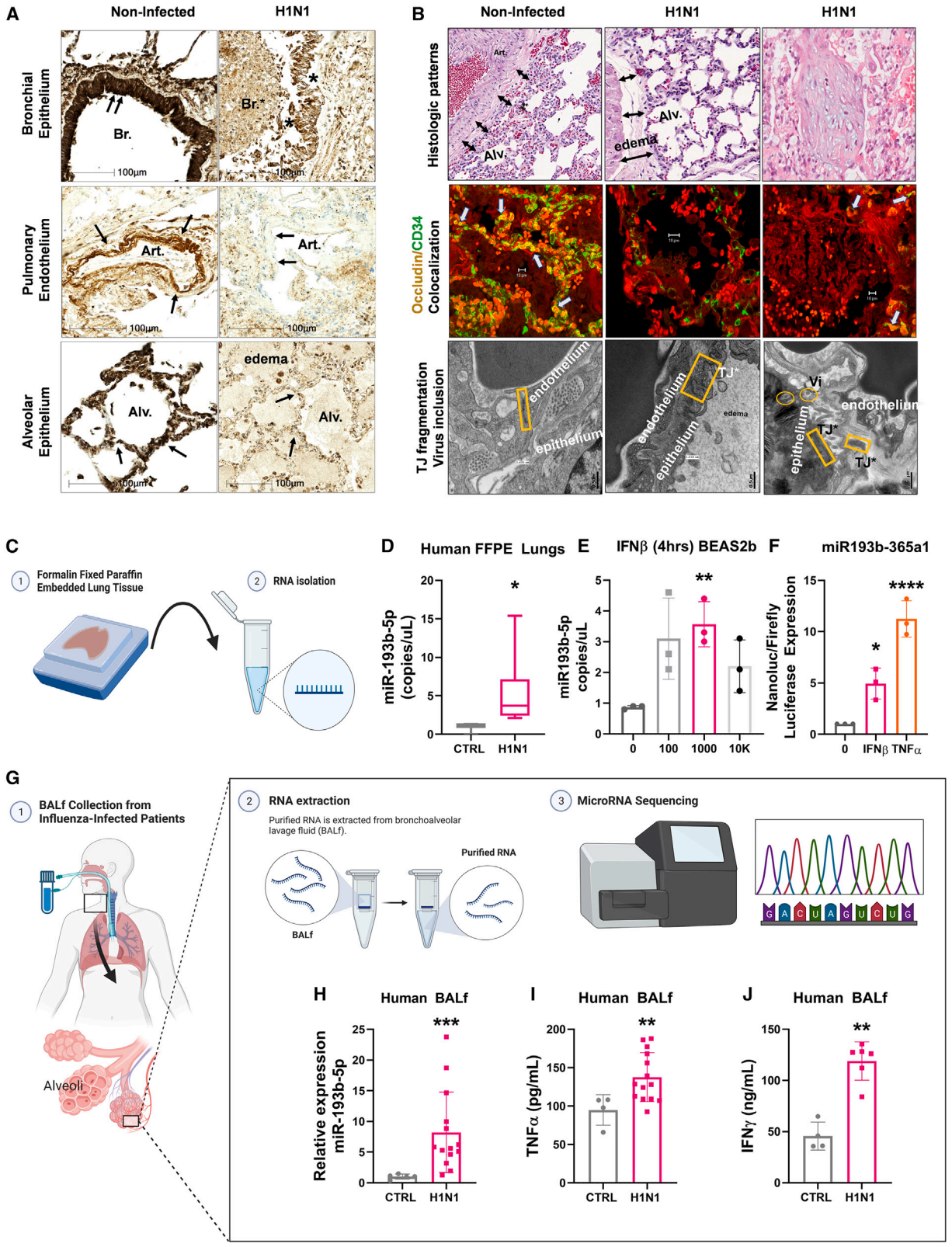

(legend on next page)

Alveolar-capillary damage[1,4] in virus-induced ARDS is associated with injury to tight junctions (TJs).[8] TJs are dynamic multiprotein complexes that function as paracellular gates that restrict diffusion between compartments on the basis of size and charge.[9–11] Beyond barrier protection, TJs transmit signals to the cell interior that regulate the cytoskeleton, gene expression, cell proliferation and differentiation, affecting various cellular processes including microbial pathogenesis.[11–13] Various pathogens have developed elegant strategies to disrupt TJs in order to reach their receptors and alter the host's immune responses, while others utilize TJ proteins as receptors for entry into cells.[14] Disruption of TJs, including occludin (Ocln), leads to increases in paracellular permeability and polarity defects which facilitate viral or bacterial cell entry and spread.[15,16] Evidence supports the role of Ocln, and associated structural proteins as targets for various classes of viruses. Ocln is a receptor for the hepatitis C virus (HCV),[5,17] coxsackievirus,[18] porcine epidemic diarrhea virus,[19] and *Toxoplasma gondii*.[20] Ocln may also affect virus pathogenicity by regulating viral replication as Ocln-deficient cells are resistant to HCV infection[5] and Ocln-targeting antibodies prevent HCV infection *in vitro*[21] and *in vivo*.[22] In contrast, IVs,[23] West Nile virus,[24] and rotaviruses[25] disrupt TJs by causing a decrease in Ocln protein expression facilitating viral entry into cells. However, the molecular mechanisms of IV-induced Ocln decrease, its effects on lung injury, and the impact of preserving Ocln in acute virus-induced lung injury remain largely unknown.

MicroRNAs (miRs) are small (~22 nucleotides) non-coding RNAs that regulate gene expression at the post-transcriptional level.[26] MicroRNAs can regulate TJ expression, modulate epithelial/endothelial barrier function and can be used directly or indirectly to augment viral replication potential.[27,28] We have recently identified miR-193b-5p, as a miR that binds to the 3′ untranslated region (UTR) of the Ocln mRNA, causing decreases in Ocln in sepsis-induced lung injury.[28] miR-193b has been implicated in viral infection,[29,30] cell-cycle regulation,[31] tumor suppression,[32] fat metabolism,[33] and vasculogenesis.[34] Whether miR-193b-5p contributes to IV-induced lung injury remains to be determined. Here, we found that in lungs from patients who died with ARDS, expression levels of miR-193b-5p are increased, while Ocln is decreased at early, as well as late stages of IV-associated ARDS. In a murine model of H1N1 influenza (PR8), miR-193b-5p inhibition prevents loss of Ocln; enhances interferon beta (IFN-β) and interferon regulated genes (IRGs) expression, reduces viral replication, histological evidence of lung injury and mortality. Silencing of Ocln reconstituted the wild-type (WT) injurious phenotype in miR-193b-deficient mice. Taken together, our work suggests Ocln plays a fundamental role in the pathogenesis of IV infection and lung injury; and that inhibition of host-derived miR-193b-5p may enhance interferon antiviral responses, prevent Ocln TJ disruption attenuating viral load and influenza-induced lung injury.

RESULTS

Decreased Ocln protein, TJ disruption, and miR-193b-5p expression in lung biopsies from patients with IV-induced ARDS

Analysis of differentially expressed genes from IV-infected vs. non-infected human lung tissue samples (GEO accession no. GSE163959) identified miR-193b as the most likely miRs regulating the gene expression pattern seen in lungs from IV-infected patients compared with non-infected controls (adjusted p value of 2.7×10^{-11}, Figure S1A). Human lung biopsies from IV-infected patients showed distinct pathological features of ARDS and reduced Ocln protein compared with non-infected controls in pulmonary bronchial epithelial, endothelial, and alveolar epithelial cells (Figure 1A, clinical data presented in Table 1). In three representative patients, IV infection demonstrated transudative edema and granulomatous tissue (Figure 1B, top panel) and showed reduced Ocln

Figure 1. Tight junctions are disrupted, mi-193b-5p expression is increased, while occludin protein is decreased in lung biopsies from patients infected with influenza virus

(A) Immunohistochemistry shows marked reduction in occludin DAB staining in influenza-infected human lung tissues compared with non-IV infected control lungs in pulmonary bronchial epithelial, endothelial, and alveolar epithelial cells. (B) Photomicrographs of three representative human histological lung sections comparing non-infected lung biopsies with the IV-induced features of acute respiratory distress syndrome (ARDS) and organizing phase pneumonia. Top panel: hematoxylin and eosin (H&E) staining showing progressive histological changes: intimate association between the basal lamina and the epithelial cells (top left); diffuse alveolar damage (DAD) and acute alveolar edema (top middle); organized or proliferative changes (top right). Middle panel: immunofluorescent staining showing co-localization of occludin (yellow, white arrows) with CD34 (green, white arrows, middle left), and occludin staining reduction in areas of acute DAD (middle mid). Progressive changes associated with increase in granulation tissue deposition is associated with decrease in the staining intensity for occludin (middle right). Bottom panel: transmission electron microscopy (TEM) images demonstrated preservations in tight junctions in the absence of viral infection (bottom left). In the acute stages of viral-induced DAD, tight junction disruptions can be seen at the apical sides between endothelial and epithelial cells associated with intra-alveolar edema (bottom middle). Disruptions of tight junctions at the ultrastructure level in the acute stage of viral-induced DAD (bottom middle). Viral particles can be seen free, adjacent to peripheral apical junctions and lateral to tight junctions invading the type 2 alveolar epithelium in organizing pneumonia (bottom right). The organizing phase of infection is associated with severe tight junction disruption with evidence of H1N1 viral particles invading the type 2 alveolar epithelium (bottom right). Abbreviations: tight junctions (TJ), virus (Vi). Clinical features of patients 1–5 are presented in Table 1. (C) Formalin-fixed, paraffin-embedded lung tissues were isolated for total RNA. Whisker plots showing significant increase in miR-193b-5p levels using. (D) Digital droplet PCR (ddPCR) showing increased copies/μL of miR-193b-5p comparing non-infected vs. H1N1-infected lungs (data are presented as median ± interquartile range [IQR], n = 3–7; *p < 0.05, **p < 0.01, **p < 0.001, ****p < 0.0001; Mann-Whitney). (E) Bar graph showing dose-dependent increase in miR-193b-5p expression in response to human recombinant IFN-β treatment (IU, international units, 4 h) in human bronchial epithelial cells (BEAS2b) using ddPCR (data are presented as median ± IQR; *p = 0.05, p = 0.01; Kruskal-Wallis; symbols represent results for independent experiments (n = 3–7). (F) Exogenous stimulation of the miR-193b promoter construct with recombinant IFN-β and TNF-α shows a significant increase in nanoluc/Firefly dual luciferase expression relative to promoterless backbone expression with 6 h of treatment. (G) Human bronchoalveolar lavage fluid (BALf) was collected from influenza-infected vs. non-infected patients, isolated and sequenced for microRNA measuring a significant increase in (H) miR-193b-5p expression. ELISA demonstrates significant increase in both (I) TNF-α and (J) IFN-γ (median ± IQR; *p < 0.05, **p < 0.01; Mann-Whitney).

Table 1. Clinical features of the patients

	Patients				
	Case 1 (MN)	Case 2 (AGC)	Case 3 (CMSM)	Case 4 (LO)	Case 5 (CFNM)
Age (years)	35	35	39	81	51
Sex	male	female	female	female	male
Premorbid disease	absent	absent	absent	RA	absent
Illness (days[a])	4	7	5	5	10
Oseltamir (days[a])	10	14	10	4	4
Steroids (days[a])	10	9	16	12	20
Intubation (days[a])	10	8	25	17	20
Status	alive	alive	dead	alive	dead
NPA	+	+	–	+	–
Lung biopsy	+	+	+	+	+
Lung EM	+	+	+	+	+

EM, electron microscopy for SALI associated to influenza A; RA, rheumatoid arthritis; NPA, nasopharyngeal aspirate. Case 3 was pregnant.
[a]Duration of illness or treatment.

staining in lung endothelial cells relative to non-infected control (by immunofluorescence for Ocln and colocalization with CD34, Figure 1B, middle panel). In both ARDS patients, the transmission electron microscopy images demonstrated progressive disruption of TJs over the course of infection associated with viral inclusions (Figure 1B lower panel). RNA was extracted from formalin-fixed paraffin-embedded (FFPE) biopsy lung tissues (Figure 1C) to demonstrate a 2- to 7-fold increase in miR-193b-5p (copies/μL) contained in digital droplets relative to non-infected controls (Figure 1D). Since miRs in the same gene cluster or family may be co-regulated at the transcriptional level and/or may share functional relationships by coregulating the same biological process,[35] we looked at the expression of miR-365a1, a member of the miR-193b/365a genomic cluster, and found that this was not differentially expressed in our biopsy lung tissues (Figure S1B). Using miRNAscope, we probed for miR-193b-5p *in situ* in human lung autopsy samples, and visually identified miR-193b-5p punctae within H1N1-infected lungs; in distal bronchi, in edema filled alveoli, and around pulmonary arterioles (Figure S1C). We further determined that the expression of miR-193b-5p increased in response to recombinant IFN-β by stimulating human primary distal bronchial airway epithelial cells (BEAS2b) with log-fold increasing doses of recombinant human IFN-β; the copy number of miR-193b-5p increased 3- to 5-fold over 4 h stimulation with 1,000 IU (international units) human recombinant IFN-β (1 pg = 1.2×10^2 IU, Figure 1E). To determine if the promoter of miR-193b is IFN-β responsive, we made a construct with the 5′ UTR of miR-193b and demonstrated, using luciferase fluorescence, increased promoter activity in response to IFN-β as well as TNF-α, indicating their regulation on miR-193b (Figure 1F). Independent bronchoalveolar lavage (BAL) samples obtained from IV-infected patients, compared with critically ill non-IV-infected patients (Toronto Public Health Laboratory and Regional Ethics Committee Comité de ética de la investigación Clinica del Principado de Asturias, Spain, ref. 22/17) and were sequenced for miR gene expression (Figure 1G) and showed increases in miR-193b-5p expression. IFN-γ and TNF-α proteins were increased using ELISA on the same BALf samples (Figures 1H, 1I, and 1J, respectively).

PR8 infection in mice recapitulates hallmark pathological features of human IV-induced ARDS

We established an intranasal murine model of influenza A infection with PR8 (Influenza, Strain A/Puerto Rico/8/34 [H1N1] at 10^7 $TCID_{50}$ [50% tissue culture infectivity dose]) that recapitulated unique pathological features of human IV-induced ARDS. This model is uniformly lethal by 8 days post-infection. WT mice were infected intranasally with PR8, and lungs were analyzed at days 3, 4, 5, and 6 post-infections (Figure 2A). Macroscopically, murine lungs became progressively more congested, hemorrhagic, and hyperemic after day 3 post-infection (Figure 2B). As early as day 4 post-PR8 infection, mice exhibited prominent bronchiolar epithelial necrosis with basement membrane detachments, epithelial necrosis, and neutrophilic infiltrates consistent with severe interstitial pneumonitis. Alveolar collapse, homogeneous septal thickening with cell infiltration, and hyaline membrane resembled features of human ARDS-associated diffuse alveolar damage (Figure 2Cix, x, xi, xii). Hyperplasia of alveolar cells with viral cytopathic changes were present (Figure S2A), similar to pathological changes evident in human severe H1N1 infection (Figure 2Cv, vi, vii, viii). Histopathologic changes showed a similar degree and pattern of lung injury distribution in mice and humans (Figure S2C). Disruptions of the intercellular junctional complexes (TJ) and opening of cell-cell contacts of type II alveolar epithelial cells (yellow square) were observed in both the transmission electron micrographs of alveolar septa in mouse and human H1N1-infected lungs (Figures 2D and 2E, respectively).

Increase in miR-193b-5p decreases Ocln and MAVS in PR8-induced acute lung injury

To determine the role of miR-193b-5p in PR8-induced lung injury, C57BL/6J mice were randomized to receive PR8 or mock infection with an equal volume of saline (Figures 2A–2C). Lungs were collected daily from days 3 to 6 post-infection. Infection resulted in ≥15% weight loss and 50% mortality rate by day 6 (Figures S2A and S2B). The levels of miR-193b-5p expression increased by 2- to 8-fold by 5–6 days post-infection (Figure 2F).

We have previously shown that the sequences for human and mouse miR-193b-5p are homologous,[36] and that miR-193b-5p binds to a conserved seed sequence in the 3′ UTR of Ocln resulting in its silencing.[37] Here we noted that increased levels of miR-193b-5p and the loss of Ocln expression at days 6 and 6 post-infection (Figure 2E) were related with worsening lung injury. In independent experiments, increased levels of miR-193b-5p were confirmed using digital droplet PCR (Figure S3C). Both the miR-193b-3p sister strand

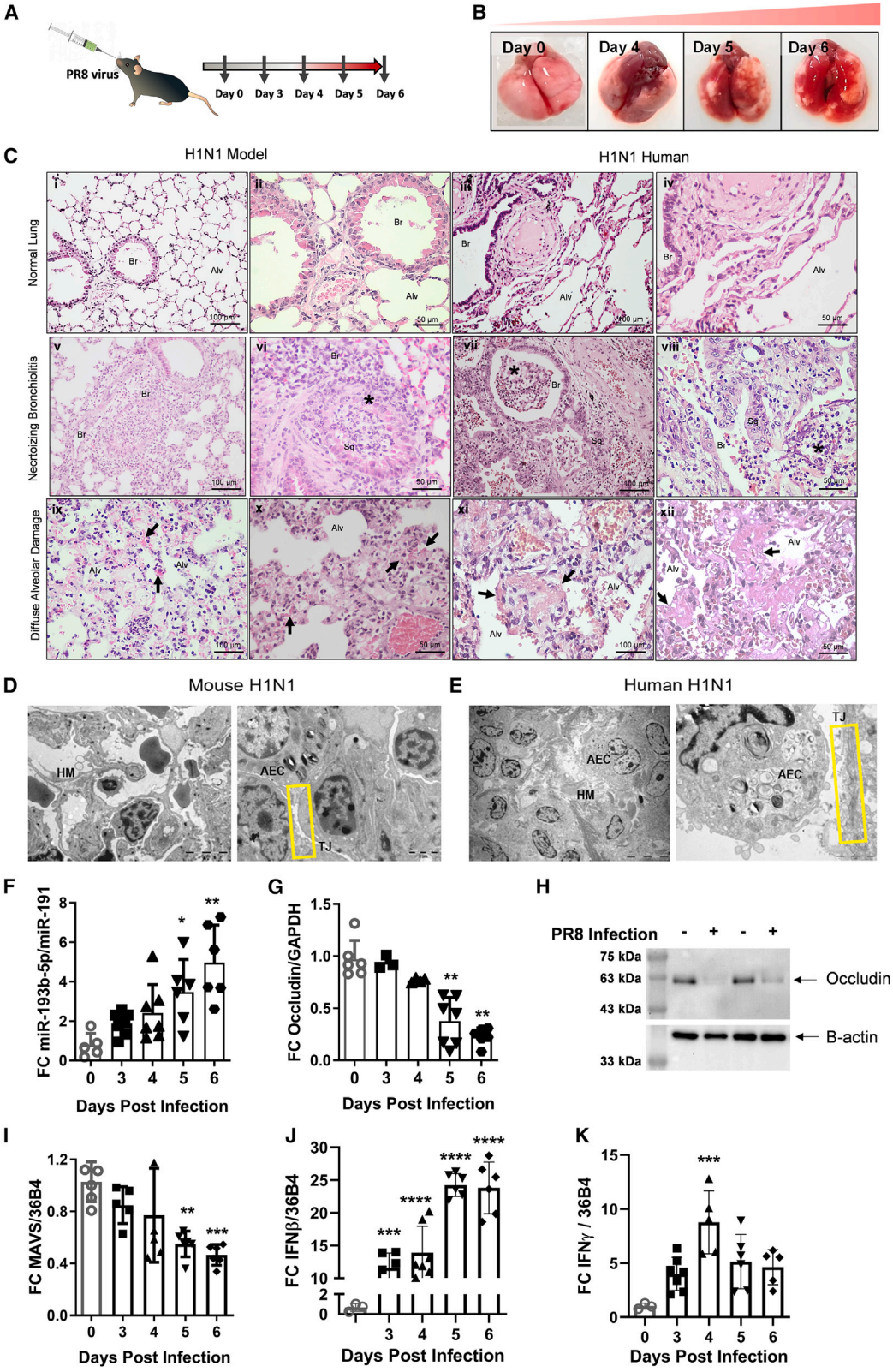

(legend on next page)

and miR-365a1-3p were not differentially expressed in our PR8 model (Figures S3D and S3E).

In addition to Ocln, the gene encoding for mitochondrial antiviral signaling (MAVS) protein is also a computationally predicted target of miR-193b-5p (MiRTarBase v.8.0). MAVS is an adaptor for the retinoic acid-inducible gene I-like receptors that mediate the transcriptional induction of type 1 interferons such as IFN-β and other IRGs that collectively establish the antiviral host response.[38] We found significant decrease in the expression of MAVS by 5–6 days post-infection (Figure 2I), but this had no impact on type 1 IFN-β gene expression. IFN-β expression increased at day 3 post-infection and continued to rise and remain elevated until mice were humanely sacrificed at day 6 post-infection (Figure 2J). Type 2 IFN, IFN-β, peaked at 4 days post-infection and remained modestly increased until day 6 post-infection (Figure 2K).

To identify which cells expressed miR-193b-5p *in vivo*, we performed *in situ* hybridization with miR-193b-5p-specific probes and co-stained for macrophages (CD64; Figure S3F), endothelial (CD34; Figure S3G), and epithelial (transcription termination factor 1 [TTF1]) (Figure S3H) cells using specific markers to demonstrate miR-193b-5p punctae within all three cell types by day 4 post-PR8 infection.

miR-193b-5p and Ocln inversely affect IV replication and IRG expression in human primary bronchial airway epithelial and pulmonary microvascular endothelial cells

Based on the *in situ* evidence of miR-193b-5p localization in both murine and human pulmonary epithelial and endothelial cells, miR-Ocln rescue and Ocln knockdown experiments were performed in human bronchoalveolar distal airway epithelial cells (BEAS2b) and human pulmonary microvascular endothelial cells (HPMECs).[39] Treating cells with increasing PR8 multiplicity of infection (MOI) resulted in increased miR-193b-5p expression levels in both BEAS2b (Figure S3I) and HPMECs (Figure S3J) at 24 h. BEAS2b cells were transfected with miR-193b-5p mimic (MIM), inhibitor (INH), or negative control (NC), followed by IV infection at an MOI of 1. Overexpression of miR-193b-5p in BEAS2b cells transfected with MIM resulted in increased detection of viral mRNA expression at 12 and 24 h post-infection (Figure 3). Viral RNA polymerase subunit 1 (PB1) was significantly increased at 12 h post-infection, and viral hemagglutinin (HA) was increased at 12 and 24 h post infection (Figures 3A and 3B).

In contrast, transfection with the miR-193b-5p INH resulted in decreased viral mRNA expression (HA and PB1) as early as 12–24 hpi (Figures 3C and 3D). However, we noticed an increase in HA and decreased PB1 transcripts by 48 hpi (Figure 3E). Viral plaque-forming units were significantly increased upon delivery of the miR-193b-5p MIM (shown in red) and decreased after treatment with the INH (shown in blue, Figure 3F). The absence of complementarity between the miR-193b sequence and the virus mRNAs sequences negates the possibility of direct mimicry of host miR by the virus.

Gene silencing of Ocln with an anti-Ocln siRNA enhances viral mRNA transcription and impairs IFN response *in vitro*

Since Ocln is a target of miR-193b-5p and other viruses use Ocln to mediate pathogen entry into cells, we assessed the direct effects of Ocln knockdown on IV viral mRNA expression. Decrease in Ocln protein expression was shown by western blot after transfection with Ocln siRNA compared with a scrambled siRNA in BEAS2b cells (Figure 3G) and quantitated through densitometry analysis (Figure S3K). Figure 3H shows that decreased Ocln expression was associated with increased expression of viral polymerase (PB1), HA, and neuraminidase. Silencing Ocln resulted in impaired type 1 IFN responses, increased viral load, and impairment of host antiviral response factors, including IFN-β (Figure 3I), IFN-induced protein with tetratricopeptide repeats 1 (IFIT-1) (Figure 3J), and bone marrow stromal cell antigen 2 (BST-2) (Figure 3K) compared with the mock saline controls, recapitulating the effects of miR-193-5p MIM transfection *in vitro* and the effects of miR-193b-5p MIM transfection *in vitro*.

miR-193b-5p inhibits type 1 IFN responses *in vitro*

HPMECs were treated with the miR-193b-5p INH or NC, followed by PR8 infection at an MOI of 1. Treatment with the INH resulted in increased expression of IFN-β (Figure 3L) and upregulation of other IFN-related genes—IFN regulatory factor 1 (Figure 3M), IFIT-1 (Figure 3N), and BST-2 (Figure 3O)—compared with NC. Taken together our data suggest miR-193b-5p downregulates type 1 interferon responses *in vitro*.

Figure 2. PR8 intranasal infection increases endogenous miR-193b-5p, localized in macrophages, pulmonary endothelial, and epithelial cells, associated with reduced occludin and mitochondrial antiviral signaling mRNA expression

(A) Schematic of the experiment. WT (C57/bl6 10–12 weeks) mice were infected intranasally (IN) with PR8 (Influenza, Strain A/Puerto Rico/8/34 [H1N1] at 10^7 $TCID_{50}$) and degree of lung injury was assessed at day 0 (baseline), and 3, 4, 5, and 6 post-infection (dpi). (B) Gross pathology images of lungs harvested on days 0, 4, 5, and 6 dpi showing increasing engorgement, hyperemia, and hemorrhagic changes over time. (C) Representative photomicrographs of H&E-stained lung sections (4 μm) showing lung injury in mice infected with PR8 compared with human lungs from H1N1-induced ARDS (i, ii, iii, iv). Necrotizing bronchiolitis and diffuse alveolar damage (DAD) were evident as early as 4 dpi in mice lung parenchyma, resembling pathological features of infected human tissue (v, vi, vii, viii). Prominent alveolar collapse, with intra-alveolar edema, DAD, and homogeneous septal thickening associated with inflammation and hyaline membrane deposition (ix, x, xi, xii). (D and E) Transmission electron micrographs of alveolar septa in mouse and human H1N1-treated lungs with diminishing of electron-dense materials, indicating disruptions of intercellular junctional complexes (TJ), and opening of cell-cell contacts of type II alveolar epithelial cells (AEC-II) (yellow square) were observed. HM, hyaline membranes; AEC, alveolar epithelial cells; TJ, tight junctions; Sq, squamous metaplasia. Bar graphs showing significant changes in the expression of (F) miR-193b-5p and (G) occludin (Ocln) 5–6 days post-PR8 inoculation in mice whole lungs. (H) Western blot demonstrating reduced occludin protein expression in mice lungs 6 days post influenza infection. Bar graphs showing significant changes in the expression of (I) mitochondrial antiviral signaling protein (MAVS), (J) IFN-β, and (K) IFN-γ in PR8-infected mice lungs relative to day 0 (n = 5–7, data are presented as median ± IQR; *$p < 0.05$, **$p < 0.01$, ***$p < 0.001$, ****$p < 0.0001$ Tukey's multiple comparisons test).

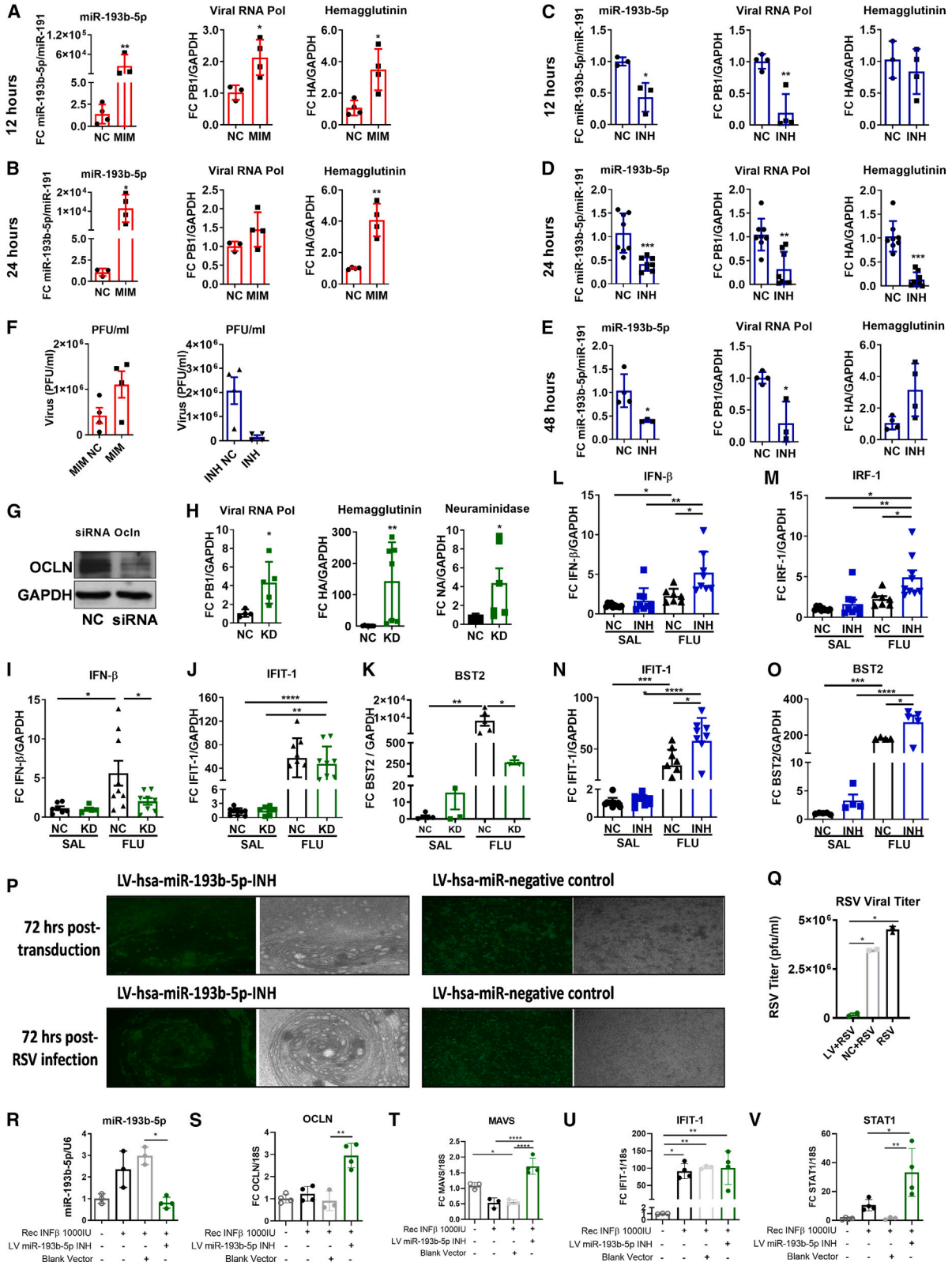

(legend on next page)

The action of miR-193b-5p on antivirus responses is not restricted to IV

To determine whether miR-193b-5p also plays a role in other important respiratory virus infection we infected primary human nasal epithelial cells (HNECs) with respiratory syncytial virus (RSV). Since HNECs are difficult to transfect, we generated a lentivirus vector overexpressing miR-193b-5p INH or empty vector (blank vector) that we used to determine the effect of miR-193b-5p inhibition in HNECs.[40] HNECs were harvested from consenting healthy volunteers and cultured in an air-fluid interface. Cells were transduced with the empty vector or the LV-miR-193b-5p-INH and allowed to differentiate for 21 days, after which they were infected with RSV. Transduction with the LV-miR-193b-5p-IHN prevented RSV infection-induced loss of normal HNEC morphology over 72 h (Figure 3P, left hand panel) compared with empty vector (Figure 3Q, right hand panel) and reduced log-fold viral titers *in vitro* (Figure 3Q), suggesting the broad applicability of the miR-193b-5p target in viral injury.

Since the lentivirus could potentially impact the IFN response, we determined the effect of the LV on IRG expression by stimulating cells transduced with either the LV-miR-193b-5p INH or empty vector with human recombinant IFN-β (1,000 IU) for 24 h. Stimulation with recombinant IFN-β resulted in increased miR-193b-5p; this was unaffected by transduction with the empty vector, but was mitigated by transduction with the LV-miR-193b-5p-INH (Figure 3R).

Ocln expression levels increased significantly in cells transduced with the LV-miR-193b-5p-INH (Figure 3S). Transduction with the empty vector did not prevent recombinant IFN-β-induced decrease in MAVS expression, while LV delivery of the miR-193b-5p INH resulted in increased MAVS expression (Figure 3T). While the expression of IFIT-1 was unaffected by LV-miR-193b-5p-INH, the expression of STAT1 was markedly enhanced by miR-193b-5p inhibition (Figures 3U and 3V). These results indicate that the role of miR-193b-5p on antivirus responses is not restricted to IV and suggest a broader applicability for miR-193b-5p inhibition for preserving or augmenting antiviral responses and decreasing viral load.

Mice deficient in miR-193b confer resistance to PR8 and have reduced lung injury and improved antiviral responses

Mice with a deletion of miR-193b (miR-193b-365a1 knockout [KO]) or their WT littermates were randomized to receive intranasally 30 μL of PR8 at 10^7 $TCID_{50}$ or equal volume saline (mock infection) and were followed for 6 days. Absence of miR-193b conferred resistance to PR8-induced morbidity, as documented by reduced change in percent loss of body weight (Figure S3L) and body temperature (Figure S3M), and an overall reduced hyperemic lung (Figure 4A). In an independent experiment, *in situ* hybridization for miR-193b-5p shows increased visible punctae in the lung parenchyma from WT mice appearing at 6 days post-infection (Figure 4B). miR-193b KO mice were included as a NC. RNU6 stained intensely in the lung tissues as a positive control for the assay, and the scrambled control was used to demonstrate the specificity of the assay with minimal to no visible punctates.

Progression of PR8-induced lung injury was markedly attenuated in miR-193b KO mice. Common histopathological features of severe human IV lower respiratory tract infection, including diffuse alveolar damage (Figure 4C) with hyaline membrane formation, patchy interstitial lymphoplasmacytic infiltrates, bronchiolitis with squamous metaplasia, and/or pulmonary congestion with various degrees of hemorrhage,[7,41] were significantly reduced in miR-193b KOs (Figure S4).

Seven-day mortality was significantly decreased in miR-193b KO mice (Figure 4D) compared with WT PR8-infected mice. At day 6 post-infection, miR-193b KO mice had decreased markers of lung injury including lower BALf total cell infiltrates, protein exudation (Figures 4E and 4F), and percent polymorphonuclear (PMN) cells in alveolar spaces (Figure 4G). We did not detect any difference in the expression of inflammation-related cytokine IL-6 mRNA (Figure 4H). However, antiviral gene expression including miR-193b-5p targets Ocln (Figure 4I), MAVS (Figure 4J), as well as IRGs, including IFITM1 (Figure 4K), the IFN alpha and beta receptor subunit 1 (IFNAR1) (Figure 4L), and IFN-β (Figure 4L), were markedly increased in miR-193b KOs compared with WT PR8-infected mice.

Figure 3. miR-193b-5p mimic enhances virus proliferation and attenuates type 1 interferon responses while miR-193b-5p inhibition reduces viral gene expression and enhances antiviral responses

BEAS2b cells were infected with H1N1 (MOI = 1.0) 24 h after transfection with miR-193b-5p mimic (MIM), inhibitor (INH), or their respective negative controls (NCs). Samples were collected at 12, 24, and/or 48 h post-infection (hpi) for analysis. Real-time qPCR for miR-193b-5p were normalized to miR-191 levels, and viral mRNA hemagglutinin (HA), viral RNA polymerase (PB1), and neuraminidase (NA) normalized to glyceraldehyde 3-phosphate dehydrogenase (GAPDH). Bar graphs showing miR-193b-5p MIM transfection results in global increases in viral mRNA transcripts (A) 12 hpi and (B) 24 hpi. miR-193b-5p INH transfection reduces viral mRNA expression sustained to (C) 12, (D) 24, and (E) 48 hpi. (F) Transfection of the miR-193b-5p MIM increases while the INH reduces viral titers at 24 h (plaque-forming units, PFU/mL). (G) Representative western blot demonstrating knockdown (KD) of Ocln using a specific siRNA against Ocln. (H) Increased PB1, HA, and NA viral transcripts after Ocln KD. Bar graphs showing decreased expression of (I) IFN-β, (J) interferon-induced protein with tetratricopeptide repeats 1 (IFIT-1), and (K) bone marrow stromal cell antigen 2 (BST2) after Ocln KD. HPMECs infected with H1N1 (MOI = 1.0) or mock infected (saline [SAL]) 24 h after transfection with INH. Bar graphs show increased expression of IFN-β and interferon-regulated genes (IRGs) (L) IFN-β, (M) interferon regulatory factor 1 (IRF-1), (N) IFIT-1, (O) BST2. Primary human nasal epithelial cells (HNECs) transduced with lentivector overexpressing the miR-193b-5p INH or negative control (NC). Three weeks (21 days) after transduction cells were infected with respiratory syncytial virus (RSV) (n = 3) and assessed after 72 h. (P) GFP fluorescent photomicrographs of NECS transduced with the LV overexpressing the miR-193b-5p INH, the empty LV, or the negative control before RSV infection, and at 72 h after RSV infection (5× and 10× magnification). (Q) Overexpression of miR-193b-5p INH significantly reduced viral load 3 days after RSV infection. (R–V) BEAS2b cells were stimulated with human recombinant IFN-β at 1,000 IU and infected with LV-miR-193b-5p INH or blank vector (empty LV) resulting in increased miR-193b-5p (R), and decreased expression of Ocln (S), MAVS (T), and IFIT-1 (U), and signal transducer and activator of transcription 1 (STAT1) (V). Data are presented as median ± IQR. Data are presented as median ± IQR; individual symbols represent results for each independent experiment (n = 3–8). Comparisons between two groups (Mann-Whitney), multiple groups (Kruskal-Wallis), and for data that were normally distributed (Kolmogorov-Smirnov): Tukey's test (*$p < 0.05$, **$p < 0.01$, ***$p < 0.001$).

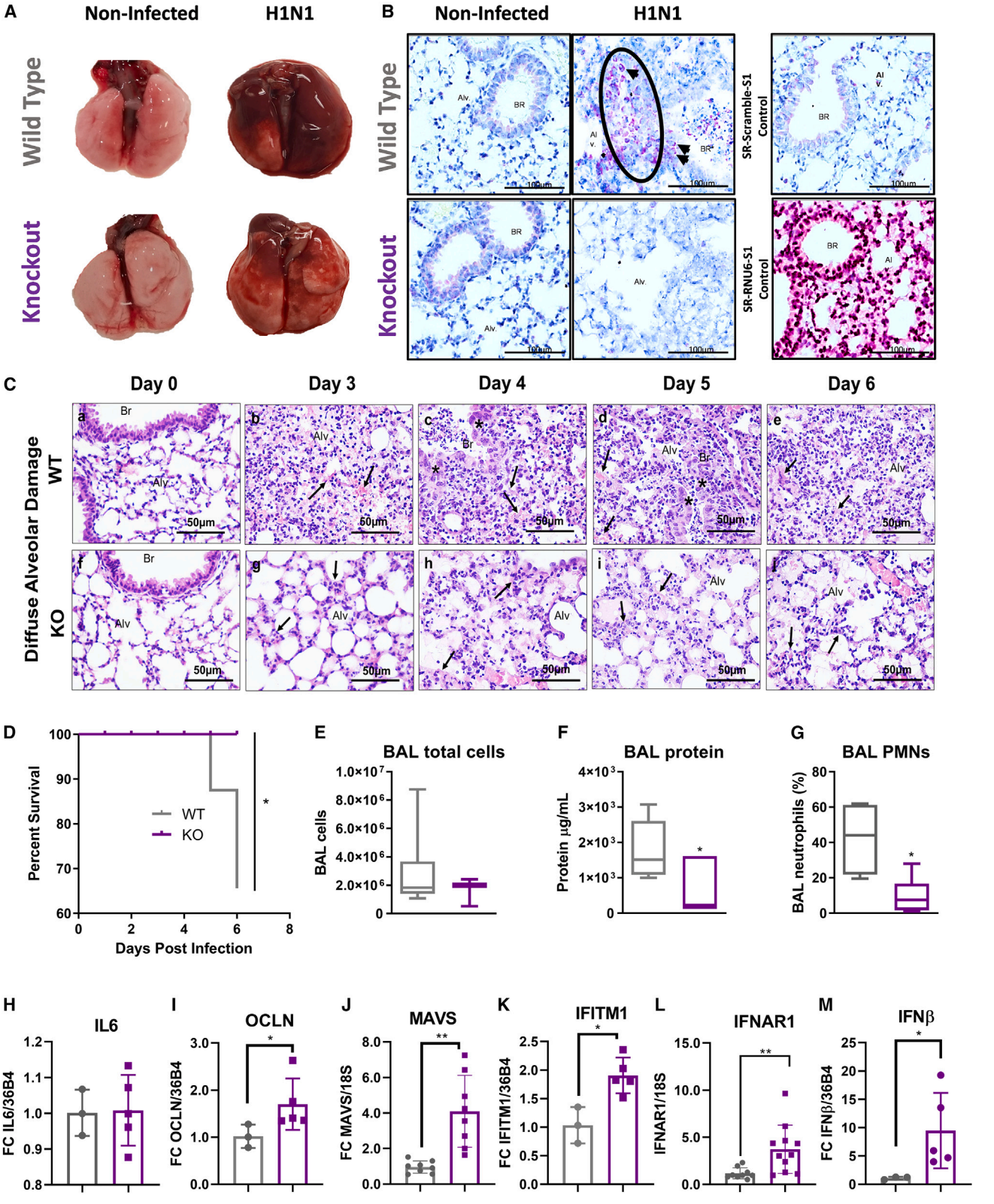

(legend on next page)

Decreased viral inclusions, preserved Ocln protein levels, and TJ integrity in PR8-infected miR-193b KO mice

Transmission electron micrography of lungs collected at day 6 post-PR8 infection from WT and miR-193b KO mice demonstrated that intercellular junctional complexes were markedly disrupted in WT mice (Figures 5A and 5B; Figure 5K, red arrows) with marked opening of alveolar epithelial cell-cell contacts (Figures 5A and 5B; Figure 5G, black arrows). Importantly, viral particles were seen totally free in cytoplasm adjacent to disrupted TJs (Figures 5A and 5B; Figure 5C, red arrows) contrasting with well-enclosed viral particles adjacent to non-fragmented TJs in miR-193b KO lungs (Figures 5A and 5B; Figure 5D, red arrows). Semiquantitative analysis of lung injury score performed by a lung pathologist (blinded to genotype and group assignment) supported preservation of alveolar epithelial cell (Figure 5C), adherens junction integrity (Figure 5D), TJs (Figure 5E), and was associated with significant reductions in viral inclusions (Figure 5F) in miR-193b KO mice compared with WT on days 4, 5, and 6 post-infection.

Ocln protein expression was preserved in miR-193b KO compared with WT mice. Ocln expression was decreased in bronchial epithelial cells by immunohistochemistry in WT mice infected with PR8 (Figure 5G); immunoblotting for Ocln confirmed preservation of Ocln in PR8 infected miR-193b KO mice compared with WTs (Figure 5H). Interestingly, immunoblotting for MAVS revealed that absence of miR-193b did not protect from PR8-induced decrease in MAVS protein expression, suggesting that, while MAVS may be a computational target of miR-193b-5p, other mechanisms may be responsible for the reduction in MAVS protein expression *in vivo* (data not shown).

These results demonstrate that absence of miR-193b results in preserved Ocln mRNA and protein expression, reduced TJ morphological disruptions, reduced loss of compartmentalization of virus particles, improved antiviral responses, and decreased lung injury and mortality post-PR8 infection.

Ocln gene silencing reconstitutes susceptibility to PR8 infection in miR-193b KO mice

To determine if Ocln is a critical target of miR-193b-5p playing a direct role in PR8-induced acute lung injury we randomized miR-193b KO mice and WT littermates to intubation and intratracheal delivery of 1.5 nmol of an anti-Ocln siRNA 24 h before intranasal inoculation with PR8 or saline (mock infection). We monitored behavioral and physiological parameters of mouse wellbeing daily and harvested lungs for analysis 5 days post-infection (Figure 6A).

Gross lung morphology showed that miR-193b KO lungs treated with the siRNA against Ocln were markedly hyperemic, consistent with severe pulmonary hepatization similar to WT littermate positive controls. In contrast, miR-193b KOs randomized to receive the scrambled siRNA were protected from PR8-induced lung injury (Figure 6B). Silencing Ocln in miR-193b KO mice infected with PR8 resulted in increased loss of percent body weight (<5%) and temperature (<5%) relative to scrambled control (Figures 6C and 6D) associated with increased mortality. Lung Ocln transcripts were significantly reduced in both WT and miR-193b KO mice treated with the siRNA against Ocln relative to scrambled control (Figure 6E), demonstrating successful knockdown of Ocln. Lung IFN-β levels significantly decreased in mice where we knocked down Ocln in WT and KO mice treated with the siRNA (Figure 6F). Lung MAVS expression in KO mice treated with the siRNA against Ocln was significantly decreased, with a non-significant decrease in the WT mice (Figure 6G). Severe IV infection induced activation of innate immune cells neutrophils and macrophages, which increases the expression of inducible nitric oxide synthase (iNOS).[42] Lung iNOS was elevated in both genotypes that received the siRNA against Ocln relative to scrambled controls (Figure 6H), suggesting increased inflammation following Ocln knockdown.

Histological assessments of lung injury were consistent with progression of lung injury following Ocln silencing in both genotypes (Figures 6I and 6J). Analysis of BALf demonstrated increased total cell infiltration (Figures 6K and 6L), PMN cells (Figure 6M), and total protein influx (Figure 6N). While Ocln silencing in WT mice non-significantly increased viral load in whole-lung tissue homogenates relative to scrambled control, the injurious effects were significantly reconstituted in miR-193b KOs (Figure 6O). Collectively, these results demonstrate that silencing Ocln in miR-193b KO mice abrogates the protective effects of miR-193b deletion and partially reverts the lung injury phenotype back to that seen in WT controls infected with PR8. Taken together, the data underscore the importance of both miR-193b and Ocln in PR8-induced acute lung injury.

Figure 4. miR-193b KO mice are protected against loss of occludin, tight junction disruption, lung injury, and PR8-induced mortality

(A) Whole-lung images between non-infected vs. 6 days PR8-infected WT lungs vs. miR193b KO mice showing less-prominent pulmonary hepatization. (B) *In situ* images showing increase in miR-193b-5p clusters (oval) and punctae (arrows) in murine lungs at 6 days post-PR8 infection vs. non-infected in WT mice relative to miR193b KO mice controls. RNU6 stained intensely as a positive control, and the scrambled control showed no visible punctates, demonstrating the specificity of the assay. (C) Mouse lung histology stained for routine H&E demonstrates extensive diffuse alveolar damage relative to miR193b KO mice. (D) Survival curve demonstrates significant survival advantage of miR-193b KO compared with WT littermates infected with PR8 (n = 5–6 per group, $TCID_{50}$ of 10^7, log rank, **p = 0.01). Comparison of PR8-induced lung injury in miR-193b KO vs. WT littermates as demonstrated by bronchoalveolar lavage fluid (BALf). (E) Trend in decreased total cells, (F) reduced protein content, and (G) significant reduction in neutrophil infiltrates by 6 dpi. Real-time qPCR showed no difference in (H) IL-6 in lung tissues, but a significant increase (I) in occludin (Ocln), (J) mitochondrial antiviral signaling (MAVS), (K) interferon-induced transmembrane protein 1 (IFITM1), (L) interferon alpha and beta receptor subunit 1 (IFNAR1), and (M) interferon beta transcripts at 6 dpi. Individual symbols represent individual mice. Data are presented as median ± IQR (*p = 0.05, **p = 0.01; Mann-Whitney for two groups and Kruskal-Wallis for multiple groups).

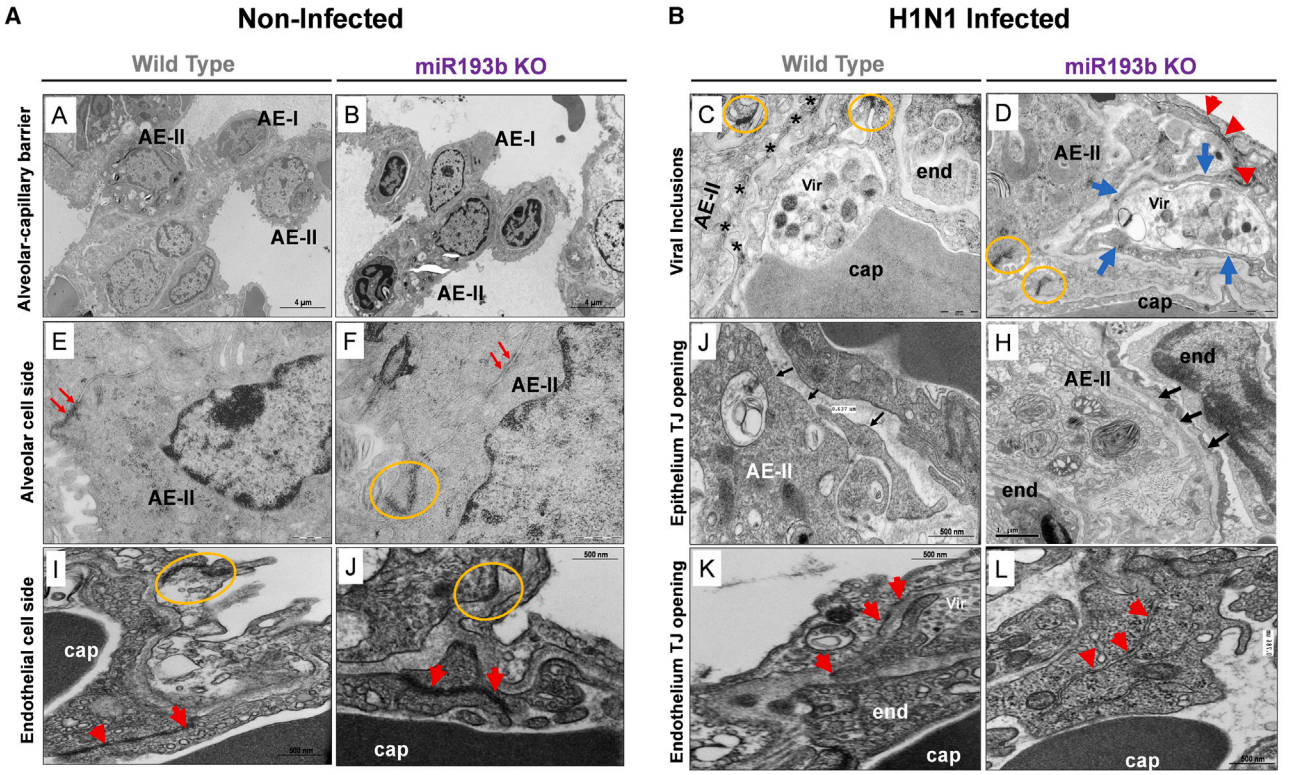

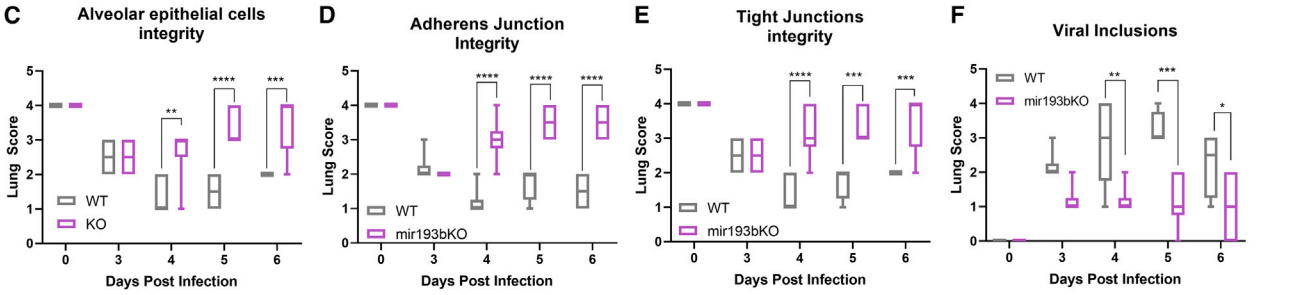

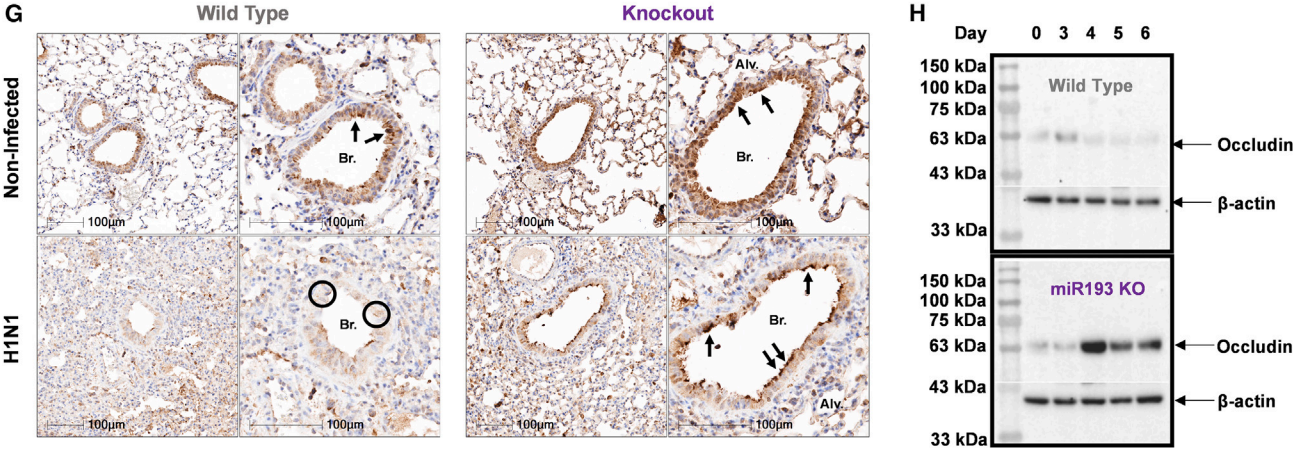

(legend on next page)

Intratracheal administration of miR-193b-5p INH mitigated loss of Ocln, reduced viral load, and improved survival in PR8-induced acute lung injury

C57/BL6 mice were randomized to receive the miR-193b-5p INH through intratracheal administration on days 4 or 5 post-PR8 infection (at 10^7 $TCID_{50}$) or the same dose of a non-human miRNA NC. A schematic of the experiment is shown in Figure 7A. Improved survival was noted when the INH was delivered on both days 4 and 5, but maximum improvement was following delivery at day 4 post-infection (Figures 7B and 7C). Lung tissues and BALf were collected on day 6 from mice treated at days 4 or 5 to determine levels of miR-193b-5p and assess lung injury-related outcomes. Treatment with miR-193b-5p INH resulted in decreased miR-193b-5p (Figure 7D), increased Ocln mRNA (Figure 7E), and protein expression (Figures 7F and 7G) in lung tissues. In addition, this treatment resulted in decreased viral titers measured using hemagglutination assay (Figure 7H), decreased expression of the viral nuclear capsid protein as measured by western blot (Figures 7I and 7J), increased IFN-β (Figure 7K), and decreased IL-6 (Figure 7L) gene expression. Infected mice treated with the miR-193b-5p INH also demonstrated decreased levels of systemic acidosis as measured by serum pH (Figure 7M) and circulating lactate (Figure 7N).

Decreased Evans blue dye incorporation in lung tissue (Figure 7O) and BALf levels of total protein (Figure 7P) and IgM (Figure 7Q) were used to demonstrate decreased exudative edema formation in mice that received the miR-193b-5p-INH compared with NC. This was associated with decreased inflammatory cell infiltration (Figure 7R), myeloperoxidase activity (Figure 7S), and NADPH oxidase 2 expression (Figure 7T). The HI perfect reagent (HPF) alone did not seem to impart significant independent effect compared with the HPF carrying the NC inhibitor (Figures S3N, S3O, and S3P), therefore our results show the comparisons of just the NC and INH. Our results show how the timeline inhibition of miR-193b-5p in a PR8 murine model, can preserve Ocln transcript and protein expression, reduce lung injury, increase IFN-β, viral clearance and improve survival *in vivo*.

DISCUSSION

MicroRNAs play a pivotal role in modulating the expression of various protein coding genes simultaneously and therefore are uniquely positioned to orchestrate a coordinated antiviral response.[43,44] Not surprisingly, viruses have developed a variety of different ways to sabotage this response.[7,8,45] Here, we demonstrate that, during IV infection, host-derived miR-193b-5p is induced by IFN-β and, in a feedback loop, acts to limit overexpression of IFN-β, which indirectly regulates the function of TJs by regulating Ocln expression levels in epithelial and endothelial pulmonary cells in a miR-193b-5p-dependent fashion. Various therapeutic strategies to silence Ocln are available for antiviral administration and are in phase 3 clinical trials to treat HCV infections.[46,47] However, strategies to preserve or modulate virus-induced disruptions of TJs and Ocln expression are not well elucidated and may be warranted for severe IV and other respiratory virus infections such as RSV. Our paper highlights the role of host-derived miR-193b-5p in the regulation of IFN-β and Ocln-dependent TJs in human cells and in mice infected with PR8. Inhibition or absence of miR-193b can mitigate H1N1- and PR8-induced cell injury and morbidity and mortality, respectively; by preserving Ocln expression and enhancing host antiviral responses.

At baseline, this miR-193b-5p is nearly undetectable; its expression *in vitro* can be induced by lipopolysaccharides (main component of Gram-negative bacteria), TNF-α,[37] and IL-1β.[48] It has been implicated in cancer metastasis,[49] angiotensin-mediated inhibition of apoptosis,[50] binding and regulation of histone deacetylase 7,[48] and Polo-like kinase 1, a critical regulator of cell-cycle progression and apoptosis.[31] Converging evidence suggests that both strands of miR-193b (-3p and -5p) play important roles in respiratory virus infections. We found that, during influenza infection, IFN-β induction of miR-193b-5p contributes to the pathogenesis of influenza through the loss of Ocln. In our models, mir-193b-5p expression levels are increased in response to recombinant IFN-β regulating the expression of other IRGs. Both IVs and other respiratory viruses such as coronaviruses (SARS/COVID) encode proteins capable of

Figure 5. miR-193b KO mice have preserved occludin and tight junction architecture with reduced viral inclusions

Representative electron microscopy tissue images showing changes in lung ultrastructure morphology in (A) non-infected (0 dpi): (left panels) the alveolar-capillary barrier ($A_{A\ and\ B}$), alveolar cell side ($A_{E\ and\ F}$), and endothelial cell side ($A_{I\ and\ J}$). (B) PR8 infected (6 dpi): PR8-infected lungs (left panels) viral inclusions ($B_{C\ and\ D}$), epithelium TJ opening ($B_{J\ and\ H}$), and endothelial TJ opening ($B_{K\ and\ L}$) WT littermate controls compared with miR-193b KO mice (N = 3). At low magnification, type I alveolar epithelial cells (AE-I) and type II AECs (AE-II) were intimately associated with each other through tight junctions (the electron-dense materials at the lateral side close to the apical surfaces, yellow circle) and adherens junctions (located adjacent to the tight junctions, black arrowheads). In PR8-infected WT lungs, a decrease in electron-dense materials indicated disruption of intercellular junctional complexes (K, red arrows) and opening of AEC cell-cell contacts (G, black arrows). In WT lungs, viral particles are totally free in the cytoplasm adjacent to disrupted TJ (C, red arrows) contrasting with well-enclosed viral particles adjacent to non-fragmented TJs in miR-93b KO lungs (D, red arrows). The sections are representative lung sections from four mice per group. Scale bars, 5 mm (low magnification) and 1 mm (high magnification). AE-I, type I alveolar epithelial cells; AE-II, type II alveolar epithelial cells; EC, endothelial cells; cap, capillaries; Vir, viral particles. Each TEM image (20 images per animal) was analyzed for alveolar epithelial cells integrity, tight junction integrity, adherens junction integrity, and viral particles at three different magnifications. Semiquantitative lung score documented significant increases in parameters for loss of (C) alveolar epithelial cell integrity, (D) adherens junction integrity, (E) tight junction integrity, and (F) significantly reduced viral inclusions in miR-193b KO mice compared with WT on 4, 5, and 6 days post-infection. Submicroscopic findings were graded according to a 5-point semiquantitative severity-based scoring system where: 0 = integrity of the submicroscopic parameters, 1 = changes in 1%–25%, 2 = changes in 26%–50%, 3 = changes in 51%–75%, and 4 = changes in 76%–100% of the examined tissue.[6] The pathologist (V.L.C.) working on the light microscopy and TEM images was blinded to group assignment. Data are presented as means ± SD (n = 4–6, two-way ANOVA, Sidak's multiple comparisons test; *p < 0.05, **p < 0.01, ***p < 0.001, ****p < 0.0001). (G) Immunohistochemistry for occludin shows miR-193b KO mice lungs have preserved occludin protein expression 5–6 days post-infection relative to WT. (H) Representative western blot demonstrated increased Ocln protein expression in miR-193b KO mice relative to WT littermates at 4–6 dpi.

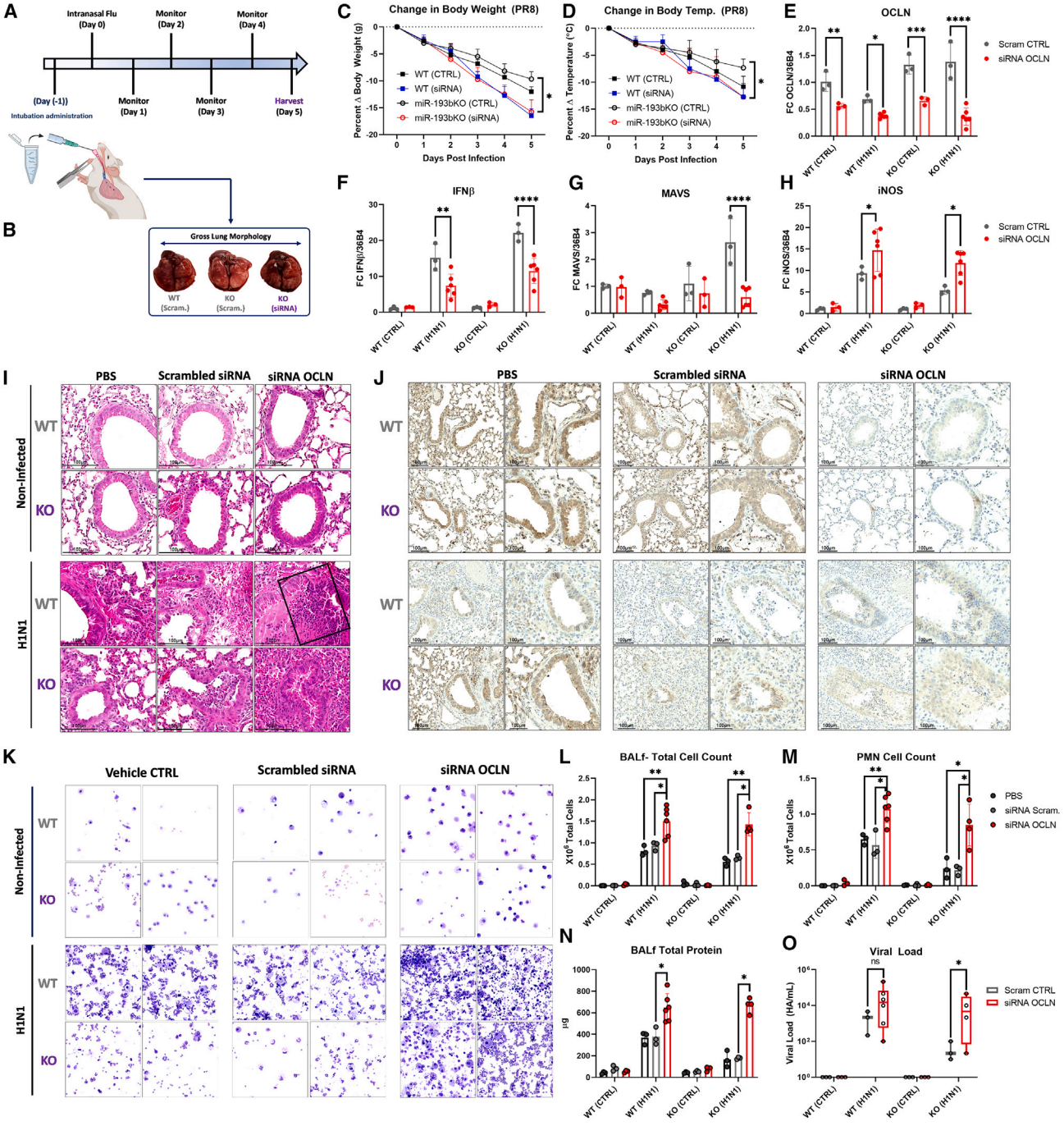

Figure 6. Knocking down occludin in miR-193b KO mice reconstitutes susceptibility to PR8-induced acute lung injury

(A) Schematic of experimental design showing intratracheal delivery of siRNA against occludin (Ocln) or scrambled siRNA 1 day before intranasal infection with PR8 ($TCID_{50}$ of 10^7). Lungs were harvested 5 dpi. (B) Gross lung pathology images showed increased pulmonary edema, hyperemia, and hemorrhagic changes in WT and miR-193b KO mice that received the siRNA against Ocln compared with miR-193b KO mice that received the scrambled siRNA. Graphs show worsening physiological parameters in WT and miR-193b KO mice that received the siRNA against Ocln (C) loss of body weight and (D) decreased body temperature. (E) Ocln knock down reduced Ocln message expression in the KO mice by about 50%; this was associated with the reduced expression of (F) IFN-β, (G) MAVS, and increased expression of (H) iNOS. Symbols represent results for individual mice; two-way ANOVA, Sidak's multiple comparisons test; *$p < 0.05$, **$p < 0.01$, ***$p < 0.001$, ****$p < 0.0001$). (I) Representative lung histology sections stained with H&E showed severe lymphocytic infiltration and alveolar collapse in miR-193b KO mice that received the siRNA against Ocln compared with non-infected WT, miR-193b KO, and mice that received the scrambled siRNA. (J) Immunohistochemistry showing decreased Ocln protein expression in siRNA-Ocln-treated miR-193b KO

(legend continued on next page)

disrupting members of the membrane-associated guanylate kinases (MAGUK) family of proteins (MUPP 1, MUPP 2, MUPP 3, and Ocln). Moreover, members of at least nine different virus families use apical-junctional complex molecules as receptors or disrupt these proteins to gain access to their receptors in the paracellular space. Naturally, multiple viruses have devised specific strategies to prevent the host from defending the apical-junctional complex as a part of their pathological mechanisms. Ocln is one of these MAGUK targets, regulated by miR-193b-5p.

Here, we show that inhibition of miR-193b-5p or miR-193b deficiency resulted in preserved Ocln levels, TJ integrity, and enhanced type 1 IFN responses, resulting in reduced lung injury and mortality. *In vitro* delivery of an siRNA against Ocln resulted in increased viral mRNA transcripts and impairment of IRG expression, demonstrating that Ocln is required for type 1 IFN responses. Electron microscopy confirms the importance of miR-193b-5p in H1N1 pathology; viral inclusions, TJ disruption, and increased paracellular spaces were significantly more prominent in WT compared with miR-193b KO mice infected with PR8. While important in regulating Ocln and IFN-β-dependent responses, our data by no means exonerate other miR-193b-5p mechanisms of action (i.e., other target genes) in influenza-induced lung injury—this is an ongoing area of research in the lab.

Gain- and loss-of-function experiments demonstrate the importance of miR-193b-5p to the regulation of IFN responses via regulation of IRGs. Although MAVS is a putative target of miR-193b-5p, our data do not support this being an effector of miR-193b-5p-induced effects since the absence of miR-193b-5p does not preclude decreases in MAVS protein expression. In addition to MAVS, various antiviral transcripts were significantly increased in miR-193b KO mice including IFITM 1 and 3. IFIT-1 proteins mediate antiviral activity against a broad range of viruses, such as influenza, through the suppression of translation initiation and sequestering viral proteins or RNA in the cytoplasm.[51,52] Emerging evidence demonstrates that IFITM1 is localized predominantly at the plasma membrane,[53] whereas IFITM2 and 3 localized within the endosomal and lysosomal compartments.[54] IFITM3 exhibits its antiviral nature by trapping virions, including influenza, in endocytic compartments, resulting in their degradation.[51,54,55] IFITM restriction is not a global property of the cell but rather localized to late or lysosomal compartments. IFITM 1, 2, and 3 have all been proven to exhibit antiviral properties including but not limited to SARS, Middle Eastern respiratory syndrome, and influenza-related viruses.[56,57] Tetherin is encoded by BST-2[58] and inhibits the release of influenza and other viruses from the surface of infected cells via induction of apoptosis.[59] The absence of IFIT-1 is not critical in influenza restriction and, similarly, the antiviral function of BST-2 can be partially antagonized.[60] IFNAR1 has recently been shown to play a critical role in other forms of respiratory virus lung infections such as infections with SARS-coronavirus 2, as inherited IFNAR1 deficiency predisposes not only to severe COVID-19 pneumonia but also multisystem inflammatory syndrome.[61]

The contribution of Ocln to permeability has been demonstrated through numerous lines of investigation: (1) blocking the extracellular loops[62,63] and reducing the protein content alters paracellular permeability,[64] (2) overexpression or prevention of Ocln degradation enhances transepithelial resistance (TER),[65] and (3) synthetic peptides mimicking the extracellular loop compete with loop-loop interactions causing increased vascular leak.[66] The debate on the role of Ocln in barrier protection centers on the fact that TJ ultrastructure appears unaltered in Ocln-deficient mice, and early studies suggested normal TER and permeability in isolated tissue preparations.[67] These initial studies, however, may not have fully appreciated the role of Ocln (and TJs) in cell signaling and cell-cell and cell-matrix functions.[68] Moreover, recent studies show that, although TJs are morphologically intact, Ocln-deficient mice have complex histological phenotypes characterized by chronic inflammation and poor TJ integrity in several epithelial/endothelial tissues, pointing to an important role for Ocln in TJ stability, signaling, and barrier function as opposed to TJ assembly.[67] Here, we did not use Ocln KO mice, primarily because current data suggest that these mice have developed alternative strategies to compensate for the absence of Ocln and therefore are not ideal for our PR8-induced acute lung injury model. Hence, we delivered an siRNA to knock down Ocln acutely *in vivo*. When we knock down Ocln in miR-193b KO mice we partially abrogate the protective effects of miR-193b deletion in mice—we think in part because Ocln expression may not be entirely sufficient to explain the decrease in vascular leakage in our model. While we investigated the role of miR-193b-5p and Ocln in an influenza viral injury model, the putative targets list for miR-193b-5p is enriched for genes encoding for proteins associated with cell-cell adhesion and cell junction assembly including claudins (CLDN-2, -19), CLCN5 (chloride channel Cl−/H+ exchanger), and non-integrin membrane-ECM interaction proteins (thrombospondin 1 and 2), which may also account for the therapeutic effect of miR-193b-5p inhibition on vascular leakage. We are currently investigating the pulmonary differential expression profile in infected vs. non-infected miR-193b KO mice vs. WT littermates. This may provide novel insights into the role of miR-193b in host-immune regulation in virus-induced ARDS.

MicroRNAs are recognized as attractive targets for intervention as their aberrant expression in various pathological contexts can play

mice associated with diffuse alveolar damage with denudation of the membrane and cellular infiltrates in the airspaces using immunohistochemistry DAB staining. (K) Representative images of cytospin showing increased (L) total cell count, (M) total neutrophil infiltrates, and (N) total protein (edema) in the bronchoalveolar lavage fluid (BALf) from mice treated with the siRNA against Ocln compared with WT and miR-193b KO treated with scrambled siRNA, recapitulating injurious WT phenotype. (O) While WT mice showed non-significant increase in viral load with the siRNA against Ocln, in miR-193b KO mice, silencing Ocln increased viral load in whole-lung tissue homogenates by 6 days post-infection relative to scrambled control treated mice (data are presented as means ± SD, n = 3–6; two-way ANOVA [Kolmogorov–Smirnov], Sidak's multiple comparisons test; *p < 0.05, **p < 0.01, ***p < 0.001, ****p < 0.0001).

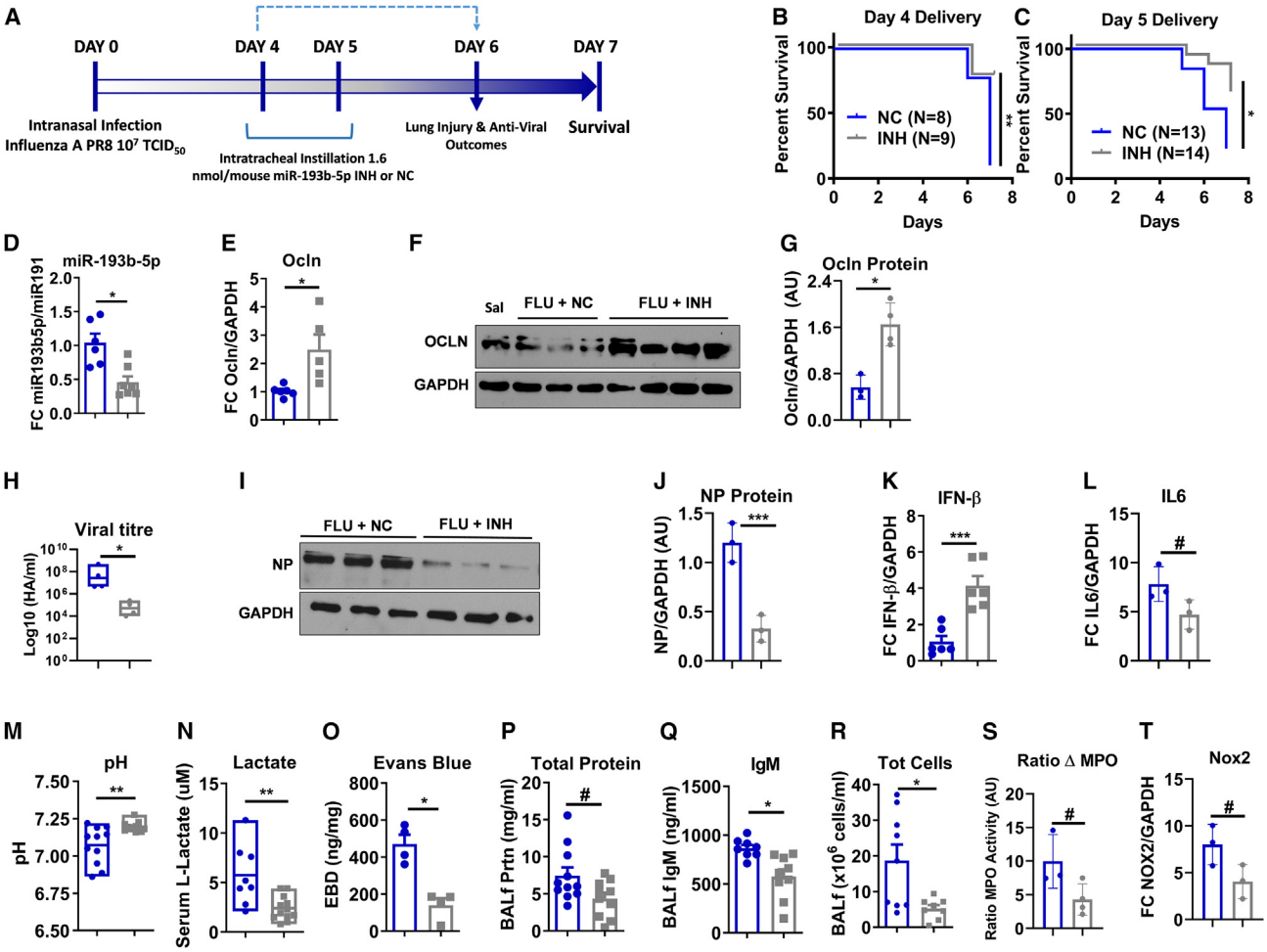

Figure 7. Inhibition of miR-193b-5p mitigates lung injury in a pre-clinical model of PR8

(A) Schematic of experimental design. C57bl6 mice (10–12 weeks) infected with H1N1 (10^7 $TCID_{50}$) were randomized to miR-193b-5p inhibitor (INH) or negative control (NC). INH and NC were delivered intratracheally (i.t.) at 4 or 5 dpi. Lungs from mice were harvested 6 dpi for lung injury assessment; a separate set of mice were followed to determine survival. Kaplan-Meier curves demonstrated survival advantage when the miR-193b-5p INH is delivered at (B) day 4 and (C) day 5 relative to NC (non-human RNA sequence, n = 8–14, log rank Mantel-Cox; *p = 0.05, **p = 0.01). Semiquantitative PCR shows significant (D) decrease in miR-193b-5p and (E) increased occludin (Ocln) transcript levels 6 dpi in miR-193b-5p INH- vs. NC-treated groups. (F) Representative western blot demonstrates increased Ocln protein expression relative to glyceraldehyde 3-phosphate dehydrogenase (GAPDH) (G) and quantified using arbitrary units (AU) between INH and NC (H), and were quantified by hemagglutination assay (HA/mL). (I) Representative western blot and (J) quantification demonstrates reduced expression of viral nuclear protein (NP) in INH relative to NC-treated H1N1 lungs. Bar graph showing significant (K) increase in IFN-β (antiviral response) and (L) decrease in inflammatory cytokine IL-6 in H1N1-infected lungs treated with the INH compared with the NC. Decreased severity of lung injury outcomes was evident at day 6 as determined by: (M) increased pH (N) decreased serum lactate (marker of systemic dysfunction), decrease in markers of pulmonary vascular leakage, and inflammation including decreased Evans blue dye incorporation into lung tissues (O) and decreased bronchoalveolar lavage fluid (P), total protein (Q), IgM levels, and total cellular infiltrates (R). (S) Significant reductions in myeloperoxidase (MPO) activity and (T) NADPH oxidase 2 (Nox2) expression levels in miR-193b-5p INH-treated lungs. Expression levels were quantified relative to GAPDH in arbitrary units (AU). Individual symbols represent results for individual mice. Data are presented as median ± IQR, Mann-Whitney U; *p < 0.05, **p < 0.01, ***p < 0.001).

critical roles in the development and progression of diseases.[69,70] In the context of virus-induced lung injury, miR command multiple gene targets,[26] and thus delivering miR mimics or inhibitors may reduce various syndromic features of lung injury and enhance survival. Synthesized single-stranded oligonucleotides (antagomirs) as well as inhibitors are showing promise as interventions for various diseases.[70] Studies have demonstrated their use in HCV,[71] chronic inflammatory diseases,[72] cardiac injury,[73] and metabolic diseases.[74] The administration of a lentivector overexpressing the miR-193b-5p INH in the presence of IFN-β rescues MAVS and Ocln, demonstrating the therapeutic potential of our inhibitor. Our findings were further supported by the overexpression of miR-193b-5p INH in a lentivector to reduce viral load and preserve TJ integrity in human primary nasal epithelial cells infected with a non-IV RSV, broadening the potential applicability of exploiting this miR in other respiratory virus disease models.

Because of their high transduction efficiency, 70% of all gene therapy clinical trials involve the use of lentiviruses (LVs). Concerns regarding high immunogenicity and the risks of insertional mutagenesis has limited the enthusiasm for translation to the clinic.[75] Enhanced safety profiles and lower production costs have led to the emergence of nonviral vectors as an attractive alternative for the delivery of synthetic siRNAs[19,75,76] and miRs.[69,70,77] Lipid nanoparticles have gained much attention for the successful delivery of therapeutic RNAs in vaccines for SARS-COV2[78,79] and treatment of hereditary amyloid transthyretin-mediated amyloidosis[80] and tuberculosis.[81,82]

In our pre-clinical *in vivo* study, cationic lipids containing the commercially available miR INH or the NC lipid micelles were generated upon mixture with the QIAGEN HPF. The miR INH was modified to reduce *in vivo* degradation (2′-O-methyl-group modified oligonucleotides). We have previously published successful delivery of our miR-193b-5p INH in an vivo model of sepsis using this methodology.[83] In this article, we show that delivery of the miR-193b-5p INH on days 4 and 5 post-infection reduces the expression levels of miR-193b-5p, 24–48 h post-inhibitor delivery. Future work will build off our proof-of-concept experiments to develop therapeutically relevant carriers, such as lipid nanoparticles, for the delivery of exogenous therapeutic miRs.

In summary, we expose the pathogenic nature of miR-193b-5p and its role in working at the behest of the virus, where its timely increase assists in the reduction of the fortified barrier-Ocln enabling a viral attack to the host system. The timely delivery of the miR-193b-5p INH, mitigates the loss of TJ Ocln, reduces viral load, and enhances host antiviral responses, thus positioning this miR as a possible novel therapeutic target in influenza-induced ARDS.

MATERIALS AND METHODS

Cell culture

Human bronchoalveolar distal airway epithelial cells (BEAS2b) were generously gifted by Dr. Haibo Zhang (University of Toronto, Canada, Department of Anesthesia). Cells were cultured in Dulbecco's modified Eagle's medium (DMEM) containing 10% fetal bovine serum (FBS) and 1% penicillin-streptomycin. HPMECs were purchased from PromoCELL (Heidelberg, Germany) and cultured in endothelial cell basal medium MV 2 (EBM-2) (CC-3202, Lonza) supplemented with endothelial cell growth medium (EGM-2MV) SingleQuot Kit supplements and growth factors (CC4176, Lonza). All *in vitro* experiments with HPMECs were performed with cells at passages 3 to 7.

In vitro miR gain- and loss-of-function experiments

Cells were incubated at 70%–80% confluency for 24 h with 5 nM syn-hsa-miR-193b-5p miScript mimic (MIM; MSY0004767), 50 nM anti-hsa-miR-193b-5p miScript miRNA INH (MIN0004767), 50 nM hsa-miRNA inhibitor NC(1027271), 75 nM occludin siRNA (Ocln KD; SI05054385), or 5 or 75 nM AllStar siRNA NC (1027280) (all purchased from QIAGEN), using HPF (301705, QIAGEN) or Lipofectamine RNAiMAX (13778150, Thermo Fisher Scientific) as per the manufacturer's instructions.

In vivo knockdown of Ocln

C57Bl6 mice were intubated 1ne day before PR8 inoculation using Ambion In Vivo Pre-Designed silencing RNA (siRNA, cat. no. 4457308) targeting Ocln, and the Ambion In Vivo Negative Control no. 1 siRNA (cat. no. 4457287). SiRNA were re-suspended with the invivofectamine 3.0 Reagent (cat. no. IVF3001), with each mouse receiving 1.6 nmol of siRNA.

Influenza infection *in vitro*

BEAS2b, Madin-Darby canine kidney (MDCK), and HPMECs cells were infected with 1.0 MOI of Influenza A/Puerto Rico/8/34 (H1N1; PR8; Charles River Laboratories) in DMEM, α-minimum essential medium (MEM), or EBM-2, respectively. Cells were supplemented with 2% FBS and 1% penicillin-streptomycin. Samples were collected at 12, 24, or 48 h post-infection.

Animal care

All experimental procedures and protocols were approved by the Animal Care Committee of St. Michael's Hospital, Toronto, ON, Canada (ACC906). Eight- to 12-week-old male C57Bl/6J WT mice were purchased from Jackson Laboratories. miR-193-365-1 knockout mice (miR-193 KO) were a generous gift from Dr. Lothar Hennighausen (National Institutes of Health). miR-193-365-1 KO mice (miR-193 KO were bred in-house at the Keenan Research Center vivarium. Generation of KO mice has been previously characterized, and the microbiome from different genotypes was not different.[84] miR-193 KO (C57Bl/6 × 129SvEv/Tac background) were bred with C57Bl/6J mice to produce heterozygotes (miR-193 Hets). DNA from ear notches was extracted using REDExtract-N-Amp (cat. no. XNAT, Sigma-Aldrich). PCR was performed per the manufacturer's instructions. Primer sequences are given in Figure S5. Primer pair 1 produces a 546 bp band in miR-193 KO animals while primer pair 2 produces a roughly 500 bp band in miR-193b WT animals. The presence of two bands, as resolved on a 3% agarose gel, indicates heterozygosity (Figure S5). All mice were housed on a standard 12 h light/dark cycle and had free access to food (Teklan Glocbal 18% Protein Rodent Diet) and reverse osmosis water. Infection experiments were performed in a biosafety level 2 (BSL-2) room in the vivarium. Non-infected mice were housed in the same BSL-2 facility room as the infected mice to minimize potential confoundment. All animals were monitored closely and treated humanely in accordance to the guidelines outlined in the Canadian Council of Animal Care. Animals were sacrificed by anesthetic overdose (isoflurane) at the endpoint of each study. Assessment of physiological parameters were performed by an experimenter blinded to the assigned groups, and welfare assessment of the mice was performed in accordance with the St. Michael's Hospital Vivarium Facility. All mice were randomized to experimental groups by providing a unique ID number per mouse in experiments, and were assigned to treatment groups using a random number generator (https://www.calculatorsoup.com) in accordance to the Animal Research: Reporting of In Vivo Experiments (ARRIVE) guidelines.[85] ARRIVE 2.0 guideline checklist is provided in the supplemental information.

Influenza infection *in vivo*

Influenza A/PR/8/34 H1N1 was grown in eggs and tissue culture infectious dose determined by infection of MDCK cells[86] and mice were anesthetized with 2%–5% isoflurane. Animals were held upright during administration. PR8 (10^7 $TCID_{50}$) in a total volume of 30 μL was administered intranasally using a pipette. Animals were then placed on a bedding-free cage on top of a heating blanket until recovery. Intratracheal instillation of oligonucleotide mixtures were performed at days 4, 5, or 6 post-infections. Formal sample size calculation based on our preliminary experiments indicates that with eight mice per group we will have a power of 0.8 (type I error of 0.5) to detect statistically significant differences in survival and BALf differential cell count between mice treated with miR-193b-5p INH vs. NC.

BALf and lung tissue harvesting

After anesthetizing the animal in 2%–5% isoflurane with continuous oxygenation, the trachea was intubated with a 20-gauge cannula, and the right main step bronchus tied off. BALf collection was performed by instilling 0.5 mL of saline into the left lung and re-aspirating the fluid three times. After cardiac puncture and exsanguination, blood was collected and immediately centrifuged for serum. The right lungs were collected, and flash frozen in liquid nitrogen for subsequent real-time qRT-PCR and protein quantification. After centrifugation, the BALf supernatant was used for protein determination using a Bradford assay. The pellet was re-suspended in PBS for total cell count using a hemocytometer and trypan blue dye. The re-suspended pellet was centrifuged onto cytospin slides, which were stained with hematoxylin and eosin with the Hemacolor Stain Set (EMD Millipore, Billerica, MA) to distinguish monocytes, neutrophils, and macrophages for subsequent cell differential analysis. Lungs were also assessed for viral load determination (plaque assay), inflammation (neutrophil count), histology, western blots, immunohistochemistry, immunoblotting, or RNA analysis.

Assessment of viral load

Standard agarose-based plaque assays were performed from the BALf. MDCK cells, an accepted tight-junction forming the epithelial cell model,[65] were maintained at 37°C in a humidified 5% CO_2 chamber under stationary conditions, cultured to 90% confluency. Each well of a 6-well plate is seeded at 1×10^6 cells and cultured in MEM (Gibco/Invitrogen, Carlsbad, CA) containing 10% FBS, 100 units/mL penicillin (Gibco), and 100 μg/mL streptomycin (Gibco). After two washes with serum-free DMEM (Gibco/Invitrogen), the cells are maintained in serum-free DMEM at 37°C for 1 h. Then, each well was overlaid with 200 μL of diluted BAL of serially diluted solutions of inoculum and incubated at 37°C for 1 h. After one wash in serum-free DMEM, the cells were overlaid with serum-free DMEM containing 0.6% agarose, 0.1% diethylamino ethyl-dextran (Sigma-Aldrich), and 7 μg/mL trypsin (Sigma-Aldrich). The cells were cultured at 37°C for 72 h, fixed in 10% formaldehyde, and then stained with 0.037% methylene blue and each experiment was performed in triplicate.

Tissue culture infectivity dose

Samples were dispensed into a clear, round-bottomed, 96-well plate and serially diluted (1:10) in replicates of four down the plate from row A to H, along with a saline only NC and a PR8-positive control. MDCK cells were seeded at 10^5 cells per well. Plates were incubated at 37°C with 5% CO_2. The following day, cells were washed twice with serum-free DMEM and incubated for 4 days with DMEM supplemented with 2% FBS, 1% penicillin-streptomycin, 1% L-glutamine, 1% NEAA, and 1× TPCK-treated trypsin. Post-incubation, 0.5% red blood cell solution was added to each well and degree of agglutination was measured after 2 h at 4°C. The $TCID_{50}$ was calculated based on the ReedMunch method.[87]

mRNA and miRNA analyses

Frozen right lungs were first homogenized using a mortar and pestle. Total RNA was then extracted from 1 mg of homogenized lung by the TRIzol Reagent (Thermo Fisher Scientific, Waltham, MA) according to the manufacturer's instructions. Complementary DNA (cDNA) was synthesized from 1 μg of RNA using the SuperScript First-Strand Synthesis System for reverse transcription (RT) PCR (Thermo Fisher Scientific, Waltham, MA) according to the manufacturer's instructions. Real-time qPCR was performed using the ViiA 7 Real-Time PCR System (Thermo Fisher Scientific). The relative change in gene expression or miRNA level was calculated by the ΔΔCT method. Gene expression was normalized to the housekeeping gene β-actin, and miR-193b-5p (QIAGEN, cat no. 339350) level was normalized to the housekeeping miRNA miR-191-5p (QIAGEN, cat no. 339350) and U6 (QIAGEN, cat no. 339350). Fold change was then normalized to appropriate controls. Primer list is provided in Table S1.

Immunoblotting protein expression

Lung tissues were homogenized, and cells were lysed using RIPA lysis buffer in loading buffer (Bio-Rad, no. 161–0737). Proteins were resolved on a 10% SDS-PAGE gel, transferred on to nitrocellulose membranes (Amersham Biosciences), and blocked in 5% milk as previously described.[88] Primary antibodies were probed overnight at 4°. Western blot bands were analyzed using Bio-Rad Gel Doc 2000. Densitometry was performed using GelQuantNet software. Antibodies used include occludin (71–1500, Invitrogen, used for tissue samples), occludin (sc-133255, Santa Cruz, used for cell samples), MAVS (no. 3993, Cell Signaling), GAPDH (no. 2118, Cell Signaling), and β-actin (sc-47778, Santa Cruz).

IFN treatment

BEAS2b cells were treated with Recombinant Human IFN-β Protein (8499-IF, R&D). The specific activity of Recombinant Human IFN-β is approximately 2.8×10^8 IU/mg, which is calibrated against human IFN-β World Health Organization International Standard (NIBSC code: 00/572). Cells were treated at log-fold increase in IFN-β. Cells were lysed with TRIzol Reagent (Thermo Fisher Scientific) and RNA was extracted 4 h post-treatment.

Lentiviral vectors overexpressing miR-193b-5p INH or NC

Third generation replication-defective and self-inactivating, VSVG-pseudotyped integrating lentivectors (LVs) were produced. Human embryonic kidney cells (HEK293T) cells were co-transfected with four plasmid vectors: (1) bicistronic LV transfer plasmid carrying

the miR-193b INH or scrambled control (NC) sequence plus the gene for green fluorescent protein (GFP), high-efficiency LV packaging, and envelope plasmids (gifts from Professor Gerard Wagemaker, University of Rotterdam) including (2) LV packaging plasmid (pMDL-g/pRRE; encoding for gag and pol proteins), (3) LV packaging plasmid (pRSV-REV; encoding for rev protein), and (4) LV envelope plasmid pMD-VSVg (encoding for VSVg: vesicular stomatitis virus glycoprotein). Viral particles were harvested 48 h post-transfection by cell supernatant centrifugation, dispersed in PBS, and stored at −80°C. Functional viral titers were calculated based on transduction of 293T cells with serial dilutions of the virus and by flow cytometry to measure percentage of GFP-positive cells. GFP expression was confirmed by microscopy and cell death by lactate dehydrogenase levels in conditioned medium.

Primary HNECs

Nasal brushings were performed from consenting healthy volunteers (REB no. 10000 61106 Hospital for Sick Children Research Ethics Board) and cells were cultured in basal epithelial growth medium. After two passages, cells were plated on collagen-coated 96-well *trans* wells for differentiation. After 21 days of growth under air-liquid interface conditions, cells were infected. Lentivirus (LV) vectors were used to transduce these cells and deliver the miR-193b-5p INH and NC sequences. At 21 days, cells were infected with PR8 (MOI = 1). Effect of miR-193b-5p inhibition was determined at 72 h post-infection. We exploited the existing system using RSV to demonstrate our approach and methodology.[40]

Digital droplet PCR

RNA (from homogenized whole lung tissue, or cells) was reverse transcribed using RT-specific TaqMan primers (cat. nos. 4427975 and 4427975, Thermo Fischer Scientific) and the TaqMan MicroRNA Reverse Transcription Kit (cat. no. 4366596, Thermo Fischer Scientific). ddPCR Supermix for Probes (cat. no. 186-3010, Bio-Rad) was used as per the manufacturer's instructions. In brief, 20 μL reaction volumes, containing 1× master mix, primers and TaqMan probes (cat. no. 4427975, Thermo Fischer Scientific), and 2 μL of cDNA were loaded on disposable droplet generator cartridges (before 12.05.2014 cat. no. 186-3008, from 12.05.2014 cat. no. 186-4008, gaskets cat. no. 186-3009, Bio-Rad). Droplets were generated with 70 μL of droplet generation oil (cat. no. 186-3005, Bio-Rad) using the QX100 system (Bio-Rad). Droplets were then transferred to a 96-well PCR plate (cat. no. 0030128.613, TwinTec, Eppendorf, Hamburg, Germany). The samples were partitioned into ∼20,000 nL sized oil droplets through a water-oil emulsion technique. Partitioned droplets were thermocycled to endpoint in a 96-well PCR plate. After PCR, the sealed plates were placed in the droplet reader from the QX100 system (Bio-Rad), and droplets were analyzed as per the manufacturer's recommendations (Droplet Reader Oil, cat. no. 186-3004). Fluorescence amplitudes were read for all droplets in each sample well in a droplet flow cytometer.

Histology

The left lung was fixed in 10% neutral-buffered formalin and embedded in paraffin. Sections (4 μm thick) were cut longitudinally from the central zone with a microtome and stained with hematoxylin-eosin for histologic analysis. Photomicrographs at magnifications of ×25, ×100, and ×400 were obtained from eight nonoverlapping fields of view per section under a light microscope (Olympus BX51, Olympus Latin America, Brazil).

miRNAscopy *in situ*

In situ hybridization for miR-193b-5p was performed using miRNAscope HD Detection Reagent-RED (cat. no. 3324510, Advanced Cell Diagnostics). The manual RNU6 (positive) control probe (cat. no. 727871-S1) and scrambled (negative) control probe (cat. no. 727881-S1) in channel S1 were used for the miRNAscope HD RED assay. The RNA-Protein Co-Detection Ancillary Kit (cat. no. 323180) allowed simultaneous co-detection of the miR-193b-5p probe (cat. no. 892401- S1), and primary antibodies TTF1 (cat. no. BS-0826R), CD34 (cat. no. PA585917), and CD68 (cat. no. PA5109344) were stained with Alexa Fluor 633 (cat. no. A21070).

Dual-Luciferase assay

The 2,800 bp of genomic sequence upstream of the human miR-193b-365a1 initiation codon (Ensembl ID ENSG00000207639) with flanking XhoI and BglII sites was synthesized by Epoch Gene into a pBluescript II SK (−) backbone. The promoter was digested using XhoI and BglII in NEB Buffer 3.1 and the fragment was cloned into the pNL1.2[NlucP] (cat. no. N1011) reporter vector. HEK293T cells were co-transfected with the promoter-reporter vector and a Firefly luciferase plasmid, pGL4.54[luc2/TK] vector (Promega) using Lipofectamine 3000 (Thermo Fisher Scientific) for 24 h. The cell culture medium was replaced with fresh DMEM medium containing Hu-IFN-β (1,000 IU) and TNF-α (10 ng/mL) at 6 h post-transfection. Mock-transfected cells were not treated with Hu-IFN-β or TNF-α. Cells were lysed, and the luciferase signal was measured using a Nano-Glo Dual-Luciferase Reporter Assay System (Promega). The results are expressed as the normalized ratio of Nanoluc to Firefly luciferase intensity in miR promoter vs. backbone only control. All experiments were repeated three times.

Ethics approval

REB no. 21-228C (St. Michael's Hospital, Toronto, Canada), REB no. 02-0118-U/05-0016-C (Toronto Public Health Laboratory, Canada), REB no. 10000 61106 (Hospital for Sick Children, Toronto, Canada), REB no. 14.048–900 (University of Sao Paolo, Brazil), and REB no. 22/17 University of Asturias, Oviedo, Spain).

FFPE human samples

Archival blocks of FFPE lung tissue from five patients who died with ARDS (two males and three females; mean age 48 years) and three control patients deceased from cancer (lung negative for malignancy: two males and one female; mean age 64 years) were obtained (CEP 14.048-900, University of Sao Paolo) and RNA was extracted from FFPE human sections using the RNeasy FFPE kit (QIAGEN, cat. no. 73504) according to the manufacturer's instructions.

Statistics analysis

All studies were randomized and blinded. Observers assessing endpoints were blinded. Formal sample size calculations are based on mortality, levels of miR-193b, or degree of lung injury. All data were analyzed using Kruskal-Wallis one-way analysis of variance (-ANOVA) or two-way ANOVA as appropriate. We used false discovery rate to correct for multiple hypothesis testing.

DATA AVAILABILITY

Data available upon request from corresponding author.

SUPPLEMENTAL INFORMATION

Supplemental information can be found online at https://doi.org/10.1016/j.ymthe.2023.06.011.

ACKNOWLEDGMENTS

We would like to thank St. Michael's Hospital Research Core Facility Staff members (Drs. Xiaofeng Lu and Caterina Di Ciano-Oliveira) and the vivarium staff for their expertise and technical support for the experiments. We further extend gratitude to Dr. Yuexin Shan, Michael Kim, Shehla Itzari, Dr. Paul Turgeon, and Dr. Ana Paula Monteiro, for their expertise and advice in the experimental models. We also thank the patients and family who donated samples for research purposes. Graphical abstract images were created with BioRender.com. This work was supported by the Canadian Institutes of Health Research (grant no. MOP-130331 to CCDS). The research reported in this publication was supported in part by the São Paulo Research Foundation (FAPESP) (2018/20403-6), Carlos Chagas Filho Foundation for Supporting Research in the State of Rio de Janeiro (FAPERJ E-26/210.181/2020), and the National Council for Scientific and Technological Development (CNPq-483005/2012-6, 401700/2020-8) and CAPES/DFATD (88881.158922/2017-01).

AUTHOR CONTRIBUTIONS

Concept and design, C.M.V., A.K.V., T.H.W., T.J.M., J.N.T., and C.C.d.S.; performed experiments and original data collection, C.M.V., A.K.V., V.L.C., S.G., A.M.E., S.Y., P.J.P., A.L.d.S., Y.C., Y.-C.T., C.C.G., S.S.-B., A.T.F., S.L.A., and A.A.; data analysis and interpretation, C.M.V., V.L.C., S.G., A.M.E., P.J.P., S.L.A., A.A., and C.C.d.S.; manuscript editing and discussion, C.M.V., A.K.V., S.G., A.M.E., J.N.T., A.L.d.S., T.H.W., C.C.G., P.R.M.R., G.M.A., T.J.M., S.S.-B., A.M., S.S.B., J.C.M., and C.C.d.S.

DECLARATION OF INTERESTS

The authors declare no competing interests.

REFERENCES

1. Luyt, C.E., Combes, A., Trouillet, J.L., Nieszkowska, A., and Chastre, J. (2011). Virus-induced acute respiratory distress syndrome: Epidemiology, management and outcome. Press. Medicale *40*, e561–e568. https://doi.org/10.1016/j.lpm.2011.05.027.

2. Taubenberger, J.K., Kash, J.C., and Morens, D.M. (2019). The 1918 influenza pandemic: 100 years of questions answered and unanswered. Sci. Transl. Med. *11*, eaau5485. https://doi.org/10.1126/scitranslmed.aau5485.

3. Dawood, F.S., Iuliano, A.D., Reed, C., Meltzer, M.I., Shay, D.K., Cheng, P.Y., Bandaranayake, D., Breiman, R.F., Brooks, W.A., Buchy, P., et al. (2012). Estimated global mortality associated with the first 12 months of 2009 pandemic influenza A H1N1 virus circulation: A modelling study. Lancet Infect. Dis. *12*, 687–695. https://doi.org/10.1016/S1473-3099(12)70121-4.

4. Short, K.R., Kroeze, E.J.B.V., Fouchier, R.A.M., and Kuiken, T. (2014). Pathogenesis of influenza-induced acute respiratory distress syndrome. Lancet Infect. Dis. *14*, 57–69. https://doi.org/10.1016/S1473-3099(13)70286-X.

5. Karginov, F.V., Hannon, G.J., Thaler, J.P., Tschöp, M.H., Michael, W., Thaler, J.P., Yi, C., Schur, E.A., Guyenet, S.J., Hwang, B.H., et al. (2015). Receptor binding and pH stability - How influenza A virus hemagglutinin affects host-specific virus infection. J. Virol. *7*, 1–7. https://doi.org/10.1016/j.lpm.2011.05.027.

6. Santos, C.L., Moraes, L., Santos, R.S., dos Santos Samary, C., Silva, J.D., Morales, M.M., Capelozzi, V.L., de Abreu, M.G., Schanaider, A., Silva, P.L., et al. (2014). The biological effects of higher and lower positive end-expiratory pressure in pulmonary and extrapulmonary acute lung injury with intra-abdominal hypertension. Crit. Care *18*, 1211–R211. https://doi.org/10.1186/cc13920.

7. Mauad, T., Hajjar, L.A., Callegari, G.D., Da Silva, L.F.F., Schout, D., Galas, F.R.B.G., Alves, V.A.F., Malheiros, D.M.A.C., Auler, J.O.C., Ferreira, A.F., et al. (2010). Lung pathology in fatal novel human influenza A (H1N1) infection. Am. J. Respir. Crit. Care Med. *181*, 72–79. https://doi.org/10.1164/rccm.200909-1420OC.

8. Armstrong, S.M., Wang, C., Tigdi, J., Si, X., Dumpit, C., Charles, S., Gamage, A., Moraes, T.J., and Lee, W.L. (2012). Influenza Infects Lung Microvascular Endothelium Leading to Microvascular Leak: Role of Apoptosis and Claudin-5. PLoS One *7*, e47323. https://doi.org/10.1371/journal.pone.0047323.

9. Anderson, J.M., Van Itallie, C.M., Peterson, M.D., Stevenson, B.R., Carew, E.A., and Mooseker, M.S. (1989). ZO-1 mRNA and protein expression during tight junction assembly in Caco-2 cells. J. Cell Biol. *109*, 1047–1056. https://doi.org/10.1083/jcb.109.3.1047.

10. Cummins, P.M. (2012). Occludin: One Protein, Many Forms. Mol. Cell. Biol. *32*, 242–250. https://doi.org/10.1128/mcb.06029-11.

11. Shirasago, Y., Shimizu, Y., Tanida, I., Suzuki, T., Suzuki, R., Sugiyama, K., Wakita, T., Hanada, K., Yagi, K., Kondoh, M., and Fukasawa, M. (2016). Occludin-Knockout Human Hepatic Huh7.5.1-8-Derived Cells Are Completely Resistant to Hepatitis C Virus Infection. Biol. Pharm. Bull. *39*, 839–848.

12. Zihni, C., Balda, M.S., and Matter, K. (2014). Signalling at tight junctions during epithelial differentiation and microbial pathogenesis. J. Cell Sci. *127*, 3401–3413. https://doi.org/10.1242/jcs.145029.

13. González-Mariscal, L., Domínguez-Calderón, A., Raya-Sandino, A., Ortega-Olvera, J.M., Vargas-Sierra, O., and Martínez-Revollar, G. (2014). Tight junctions and the regulation of gene expression. Semin. Cell Dev. Biol. *36*, 213–223. https://doi.org/10.1016/j.semcdb.2014.08.009.

14. Torres-Flores, J.M., and Arias, C.F. (2015). Tight junctions go viral. Viruses *7*, 5145–5154. https://doi.org/10.3390/v7092865.

15. Baer, A., and Kehn-Hall, K. (2014). Viral concentration determination through plaque assays: Using traditional and novel overlay systems. J. Vis. Exp. *1*, e52065. https://doi.org/10.3791/52065.

16. Paradis, T., Bègue, H., Basmaciyan, L., Dalle, F., and Bon, F. (2021). Tight junctions as a key for pathogens invasion in intestinal epithelial cells. Int. J. Mol. Sci. *22*, 1–21. https://doi.org/10.3390/ijms22052506.

17. Benedicto, I., Molina-Jiménez, F., Bartosch, B., Cosset, F.-L., Lavillette, D., Prieto, J., Moreno-Otero, R., Valenzuela-Fernández, A., Aldabe, R., López-Cabrera, M., and Majano, P.L. (2009). The Tight Junction-Associated Protein Occludin Is Required for a Postbinding Step in Hepatitis C Virus Entry and Infection. J. Virol. *83*, 8012–8020. https://doi.org/10.1128/JVI.00038-09.

18. Coyne, C.B., Shen, L., Turner, J.R., and Bergelson, J.M. (2007). Coxsackievirus Entry across Epithelial Tight Junctions Requires Occludin and the Small GTPases Rab34 and Rab5. Cell Host Microbe *2*, 181–192. https://doi.org/10.1016/j.chom.2007.07.003.

19. Luo, X., Guo, L., Zhang, J., Xu, Y., Gu, W., Feng, L., and Wang, Y. (2017). Tight Junction Protein Occludin Is a Porcine Epidemic Diarrhea Virus Entry Factor. J. Virol. *91*, e00202-17–e00214. https://doi.org/10.1128/jvi.00202-17.

20. Briceño, M.P., Nascimento, L.A.C., Nogueira, N.P., Barenco, P.V.C., Ferro, E.A.V., Rezende-Oliveira, K., Goulart, L.R., Barbosa, B.d.F., Alves, P.T., Lima, W.R., and Silva, N.M. (2016). Toxoplasma gondii Infection Promotes Epithelial Barrier

Dysfunction of Caco-2 Cells. J. Histochem. Cytochem. *64*, 459–469. https://doi.org/10.1369/0022155416656349.

21. Okai, K., Ichikawa-Tomikawa, N., Saito, A.C., Watabe, T., Sugimoto, K., Fujita, D., Ono, C., Fukuhara, T., Matsuura, Y., Ohira, H., and Chiba, H. (2018). A novel occludin-targeting monoclonal antibody prevents hepatitis C virus infection in vitro. Oncotarget *9*, 16588–16598. https://doi.org/10.18632/oncotarget.24742.

22. Shimizu, Y., Shirasago, Y., Kondoh, M., Suzuki, T., Wakita, T., Hanada, K., and Yagi, K. (2018). crossm Monoclonal Antibodies against Occludin Completely *92*, 1–19.

23. Short, K.R., Kasper, J., Van Der Aa, S., Andeweg, A.C., Zaaraoui-Boutahar, F., Goeijenbier, M., Richard, M., Herold, S., Becker, C., Scott, D.P., et al. (2016). Influenza virus damages the alveolar barrier by disrupting epithelial cell tight junctions. Eur. Respir. J. *47*, 954–966. https://doi.org/10.1183/13993003.01282-2015.

24. Xu, Z., Waeckerlin, R., Urbanowski, M.D., van Marle, G., and Hobman, T.C. (2012). West nile virus infection causes endocytosis of a specific subset of tight junction membrane proteins. PLoS One *7*, 378866–e37911. https://doi.org/10.1371/journal.pone.0037886.

25. Beau, I., Cotte-Laffitte, J., Amsellem, R., and Servin, A.L. (2007). A Protein Kinase A-Dependent Mechanism by Which Rotavirus Affects the Distribution and mRNA Level of the Functional Tight Junction-Associated Protein, Occludin, in Human Differentiated Intestinal Caco-2 Cells. J. Virol. *81*, 8579–8586. https://doi.org/10.1128/jvi.00263-07.

26. Takeda, A., Iwasaki, S., Watanabe, T., Utsumi, M., and Watanabe, Y. (2008). The mechanism selecting the guide strand from small RNA duplexes is different among Argonaute proteins. Plant Cell Physiol. *49*, 493–500. https://doi.org/10.1093/pcp/pcn043.

27. Guo, Y.E., and Steitz, J.A. (2014). Virus Meets Host MicroRNA: the Destroyer, the Booster, the Hijacker. Mol. Cell. Biol. *34*, 3780–3787. https://doi.org/10.1128/mcb.00871-14.

28. Dos Santos, C.C., Amatullah, H., Vaswani, C.M., Maron-Gutierrez, T., Kim, M., Mei, S.H.J., Szaszi, K., Monteiro, A.P.T., Varkouhi, A.K., Herreroz, R., et al. (2022). Mesenchymal stromal (stem) cell therapy modulates miR-193b-5p expression to attenuate sepsis-induced acute lung injury. Eur. Respir. J. *59*, 2004216. https://doi.org/10.1183/13993003.04216-2020.

29. Makkoch, J., Poomipak, W., Saengchoowong, S., Khongnomnan, K., Praianantathavorn, K., Jinato, T., Poovorawan, Y., and Payungporn, S. (2016). Human microRNAs profiling in response to influenza A viruses (subtypes pH1N1, H3N2, and H5N1). Exp. Biol. Med. *241*, 409–420. https://doi.org/10.1177/1535370215611764.

30. Yang, X., Zhao, C., Bamunuarachchi, G., Wang, Y., Liang, Y., Huang, C., Zhu, Z., Xu, D., Lin, K., Senavirathna, L.K., et al. (2019). miR-193b represses influenza A virus infection by inhibiting Wnt/β-catenin signalling. Cell. Microbiol. *21*, e13001–e13020. https://doi.org/10.1111/cmi.13001.

31. Shin, C.H., Lee, H., Kim, H.R., Choi, K.H., Joung, J.G., and Kim, H.H. (2017). Regulation of PLK1 through competition between hnRNPK, miR-149-3p and miR-193b-5p. Cell Death Differ. *24*, 1861–1871. https://doi.org/10.1038/cdd.2017.106.

32. Moore, C., Parrish, J.K., and Jedlicka, P. (2017). MiR-193b, downregulated in Ewing Sarcoma, targets the ErbB4 oncogene to inhibit anchorage-independent growth. PLoS One *12*, 01780288–e178112. https://doi.org/10.1371/journal.pone.0178028.

33. Meerson, A., Traurig, M., Ossowski, V., Fleming, J.M., Mullins, M., and Baier, L.J. (2013). Human adipose microRNA-221 is upregulated in obesity and affects fat metabolism downstream of leptin and TNF-α. Diabetologia *56*, 1971–1979. https://doi.org/10.1007/s00125-013-2950-9.

34. Hulin, J.A., Tommasi, S., Elliot, D., Hu, D.G., Lewis, B.C., and Mangoni, A.A. (2017). MiR-193b regulates breast cancer cell migration and vasculogenic mimicry by targeting dimethylarginine dimethylaminohydrolase. Sci. Rep. *7*, 13996–14015. https://doi.org/10.1038/s41598-017-14454-1.

35. Wang, Y., Luo, J., Zhang, H., and Lu, J. (2016). MicroRNAs in the Same Clusters Evolve to Coordinately Regulate Functionally Related Genes. Mol. Biol. Evol. *33*, 2232–2247. https://doi.org/10.1093/molbev/msw089.

36. Artzi, S., Kiezun, A., and Shomron, N. (2008). miRNAminer: A tool for homologous microRNA gene search. BMC Bioinformatics *9*, 39–47. https://doi.org/10.1186/1471-2105-9-39.

37. Dos Santos, C. Mesenchymal Stromal (Stem) Cell (MSC) Therapy Modulates miR-193b-5p Expression to Attenuate Sepsis-Induced Acute Lung Injury.

38. Deng, J., Chen, Y., Liu, G., Ren, J., Go, C., Ivanciuc, T., Deepthi, K., Casola, A., Garofalo, R.P., and Bao, X. (2015). Mitochondrial antiviral-signalling protein plays an essential role in host immunity against human metapneumovirus. J. Gen. Virol. *96*, 2104–2113. https://doi.org/10.1099/vir.0.000178.

39. Heijink, I.H., Brandenburg, S.M., Noordhoek, J.A., Postma, D.S., Slebos, D.J., and Van Oosterhout, A.J.M. (2010). Characterisation of cell adhesion in airway epithelial cell types using electric cell-substrate impedance sensing. Eur. Respir. J. *35*, 894–903. https://doi.org/10.1183/09031936.00065809.

40. Cao, H., Ouyang, H., Ip, W., Du, K., Duan, W., Avolio, J., Wu, J., Duan, C., Yeger, H., Bear, C.E., et al. (2015). Testing gene therapy vectors in human primary nasal epithelial cultures. Mol. Ther. Methods Clin. Dev. *2*, 15034. https://doi.org/10.1038/mtm.2015.34.

41. Beasley, M.B. The Pathologist ' S Approach to Acute Lung Injury. 719–727.

42. Burggraaf, S., Bingham, J., Payne, J., Kimpton, W.G., Lowenthal, J.W., and Bean, A.G.D. (2011). Increased inducible nitric oxide synthase expression in organs is associated with a higher severity of H5N1 influenza virus infection. PLoS One *6*, 145611–e14612. https://doi.org/10.1371/journal.pone.0014561.

43. Forster, S.C., Tate, M.D., and Hertzog, P.J. (2015). MicroRNA as type I interferon-regulated transcripts and modulators of the innate immune response. Front. Immunol. *6*, 334–339. https://doi.org/10.3389/fimmu.2015.00334.

44. Bruscella, P., Bottini, S., Baudesson, C., Pawlotsky, J.M., Feray, C., and Trabucchi, M. (2017). Viruses and miRNAs: More friends than foes. Front. Microbiol. *8*, 824–911. https://doi.org/10.3389/fmicb.2017.00824.

45. Fensterl, V., and Sen, G.C. (2015). Interferon-Induced Ifit Proteins: Their Role in Viral Pathogenesis. J. Virol. *89*, 2462–2468. https://doi.org/10.1128/jvi.02744-14.

46. Lou, Z., Sun, Y., and Rao, Z. (2014). Current progress in antiviral strategies. Trends Pharmacol. Sci. *35*, 86–102. https://doi.org/10.1016/j.tips.2013.11.006.

47. Ullah, H., Hou, W., Dakshanamurthy, S., and Tang, Q. (2019). Host targeted antiviral (HTA): Functional inhibitor compounds of scaffold protein RACK1 inhibit herpes simplex virus proliferation. Oncotarget *10*, 3209–3226. https://doi.org/10.18632/oncotarget.26907.

48. Zhang, C., Zhang, Z., Chang, Z., Mao, G., Hu, S., Zeng, A., and Fu, M. (2019). miR-193b-5p regulates chondrocytes metabolism by directly targeting histone deacetylase 7 in interleukin-1β-induced osteoarthritis. J. Cell. Biochem. *120*, 12775–12784. https://doi.org/10.1002/jcb.28545.

49. Hu, S., Cao, M., He, Y., Zhang, G., Liu, Y., Du, Y., Yang, C., and Gao, F. (2020). CD44v6 targeted by miR-193b-5p in the coding region modulates the migration and invasion of breast cancer cells. J. Cancer *11*, 260–271. https://doi.org/10.7150/jca.35067.

50. Sun, Y., Zhang, S., Yue, M., Li, Y., Bi, J., and Liu, H. (2019). Angiotensin II inhibits apoptosis of mouse aortic smooth muscle cells through regulating the circNRG-1/miR-193b-5p/NRG-1 axis. Cell Death Dis. *10*, 362. https://doi.org/10.1038/s41419-019-1590-5.

51. Diamond, M.S., and Farzan, M. (2013). The broad-spectrum antiviral functions of IFIT and IFITM proteins. Nat. Rev. Immunol. *13*, 46–57. https://doi.org/10.1038/nri3344.

52. Pinto, A.K., Williams, G.D., Szretter, K.J., White, J.P., Proença-Módena, J.L., Liu, G., Olejnik, J., Brien, J.D., Ebihara, H., Mühlberger, E., et al. (2015). Human and Murine IFIT1 Proteins Do Not Restrict Infection of Negative-Sense RNA Viruses of the Orthomyxoviridae, Bunyaviridae, and Filoviridae Families. J. Virol. *89*, 9465–9476. https://doi.org/10.1128/jvi.00996-15.

53. Feng, B., Zhao, L., Wang, W., Wang, J., Wang, H., Duan, H., Zhang, J., and Qiao, J. (2017). Investigation of antiviral state mediated by interferon-inducible transmembrane protein 1 induced by H9N2 virus and inactivated viral particle in human endothelial cells. Virol. J. *14*, 213–312. https://doi.org/10.1186/s12985-017-0875-5.

54. Wang, B., Lam, T.H., Soh, M.K., Ye, Z., Chen, J., and Ren, E.C. (2018). Influenza A virus facilitates its infectivity by activating p53 to inhibit the expression of interferon-induced transmembrane proteins. Front. Immunol. *9*, 1193. https://doi.org/10.3389/fimmu.2018.01193.

55. Fassati, A. (2014). Fuse me IFITM can. Retrovirology *11*, 104–112. https://doi.org/10.1186/s12977-014-0104-x.

56. Brass, A.L., Huang, I.C., Benita, Y., John, S.P., Krishnan, M.N., Feeley, E.M., Ryan, B.J., Weyer, J.L., van der Weyden, L., Fikrig, E., et al. (2009). The IFITM Proteins Mediate Cellular Resistance to Influenza A H1N1 Virus, West Nile Virus, and Dengue Virus. Cell *139*, 1243–1254. https://doi.org/10.1016/j.cell.2009.12.017.

57. Feeley, E.M., Sims, J.S., John, S.P., Chin, C.R., Pertel, T., Chen, L.M., Gaiha, G.D., Ryan, B.J., Donis, R.O., Elledge, S.J., and Brass, A.L. (2011). IFITM3 inhibits influenza a virus infection by preventing cytosolic entry. Plos Pathog. *7*, e1002337. https://doi.org/10.1371/journal.ppat.1002337.

58. Yi, E., Oh, J., Kang, H.R., Song, M.J., and Park, S.H. (2019). BST2 inhibits infection of influenza A virus by promoting apoptosis of infected cells. Biochem. Biophys. Res. Commun. *509*, 414–420. https://doi.org/10.1016/j.bbrc.2018.12.110.

59. Hu, S., Yin, L., Mei, S., Li, J., Xu, F., Sun, H., Liu, X., Cen, S., Liang, C., Li, A., and Guo, F. (2017). BST-2 restricts IAV release and is countered by the viral M2 protein. Biochem. J. *474*, 715–730. https://doi.org/10.1042/BCJ20160861.

60. Mangeat, B., Cavagliotti, L., Lehmann, M., Gers-Huber, G., Kaur, I., Thomas, Y., Kaiser, L., and Piguet, V. (2012). Influenza virus partially counteracts restriction imposed by tetherin/BST-2. J. Biol. Chem. *287*, 22015–22029. https://doi.org/10.1074/jbc.M111.319996.

61. Abolhassani, H., Landegren, N., Bastard, P., Materna, M., Modaresi, M., Du, L., Aranda-Guillén, M., Sardh, F., Zuo, F., Zhang, P., et al. (2022). Inherited IFNAR1 Deficiency in a Child with Both Critical COVID-19 Pneumonia and Multisystem Inflammatory Syndrome. J. Clin. Immunol. *42*, 471–483. https://doi.org/10.1007/s10875-022-01215-7.

62. Tavelin, S., Hashimoto, K., Malkinson, J., Lazorova, L., Toth, I., and Artursson, P. (2003). A New Principle for Tight Junction Modulation Based on Occludin Peptides. Mol. Pharmacol. *64*, 1530–1540. https://doi.org/10.1124/mol.64.6.1530.

63. Vietor, I., Bader, T., Paiha, K., and Huber, L.A. (2001). Perturbation of the tight junction permeability barrier by occludin loop peptides activates β-catenin/TCF/LEF-mediated transcription. EMBO Rep. *2*, 306–312. https://doi.org/10.1093/embo-reports/kve066.

64. Hirase, T., Staddon, J.M., Saitou, M., Ando-Akatsuka, Y., Itoh, M., Furuse, M., Fujimoto, K., Tsukita, S., and Rubin, L.L. (1997). Occludin as a possible determinant of tight junction permeability in endothelial cells. J. Cell Sci. *110*, 1603–1613. https://doi.org/10.1242/jcs.110.14.1603.

65. McCarthy, K.M., Skare, I.B., Stankewich, M.C., Furuse, M., Tsukita, S., Rogers, R.A., Lynch, R.D., and Schneeberger, E.E. (1996). Occludin is a functional component of the tight junction. J. Cell Sci. *109*, 2287–2298. https://doi.org/10.1242/jcs.109.9.2287.

66. Nath, D. (2005). Membrane biology. Nature *438*, 577. https://doi.org/10.1038/438577a.

67. Saitou, M., Furuse, M., Sasaki, H., Schulzke, J.D., Fromm, M., Takano, H., Noda, T., and Tsukita, S. (2000). Complex phenotype of mice lacking occludin, a component of tight junction strands. Mol. Biol. Cell *11*, 4131–4142. https://doi.org/10.1091/mbc.11.12.4131.

68. Kanayasu-Toyoda, T., Ishii-Watabe, A., Kikuchi, Y., Kitagawa, H., Suzuki, H., Tamura, H., Tada, M., Suzuki, T., Mizuguchi, H., and Yamaguchi, T. (2018). Occludin as a functional marker of vascular endothelial cells on tube-forming activity. J. Cell. Physiol. *233*, 1700–1711. https://doi.org/10.1002/jcp.26082.

69. Qiu, Y., Lam, J.K.W., Leung, S.W.S., and Liang, W. (2016). Delivery of RNAi therapeutics to the airways - From bench to bedside. Molecules *21*, 1249–1332. https://doi.org/10.3390/molecules21091249.

70. Krützfeldt, J., Rajewsky, N., Braich, R., Rajeev, K.G., Tuschl, T., Manoharan, M., and Stoffel, M. (2005). Silencing of microRNAs in vivo with "antagomirs. Nature *438*, 685–689. https://doi.org/10.1038/nature04303.

71. Jopling, C.L. (2010). Targeting microRNA-122 to treat hepatitis C virus infection. Viruses *2*, 1382–1393. https://doi.org/10.3390/v2071382.

72. Tahamtan, A., Teymoori-Rad, M., Nakstad, B., and Salimi, V. (2018). Anti-inflammatory MicroRNAs and their potential for inflammatory diseases treatment. Front. Immunol. *9*, 1377–1414. https://doi.org/10.3389/fimmu.2018.01377.

73. Ektesabi, A.M., Mori, K., Tsoporis, J.N., Vaswani, C.M., Gupta, S., Walsh, C., Varkouhi, A.K., Mei, S.H.J., Stewart, D.J., Liles, W.C., et al. (2021). Mesenchymal Stem/Stromal Cells Increase Cardiac miR-187-3p Expression in a Polymicrobial Animal Model of Sepsis. Shock *56*, 133–141. https://doi.org/10.1097/SHK.0000000000001701.

74. Deiuliis, J.A. (2016). MicroRNAs as regulators of metabolic disease: Pathophysiologic significance and emerging role as biomarkers and therapeutics. Int. J. Obes. *40*, 88–101. https://doi.org/10.1038/ijo.2015.170.

75. Bulcha, J.T., Wang, Y., Ma, H., Tai, P.W.L., and Gao, G. (2021). Viral vector platforms within the gene therapy landscape. Signal Transduct. Target. Ther. *6*, 53. https://doi.org/10.1038/s41392-021-00487-6.

76. Rossi, J.J. (2006). RNAi as a treatment for HIV-1 infection. Biotechniques *40*, 25–29. https://doi.org/10.2144/000112167.

77. Cullis, P.R., and Hope, M.J. (2017). Lipid Nanoparticle Systems for Enabling Gene Therapies. Mol. Ther. *25*, 1467–1475. https://doi.org/10.1016/j.ymthe.2017.03.013.

78. Idris, A., Davis, A., Supramaniam, A., Acharya, D., Kelly, G., Tayyar, Y., West, N., Zhang, P., McMillan, C.L.D., Soemardy, C., et al. (2021). A SARS-CoV-2 targeted siRNA-nanoparticle therapy for COVID-19. Mol. Ther. *29*, 2219–2226. https://doi.org/10.1016/j.ymthe.2021.05.004.

79. Dolgin, E. (2021). How COVID unlocked the power of mRNA. Nature *589*, 189–191.

80. Kristen, A.V., Ajroud-Driss, S., Conceição, I., Gorevic, P., Kyriakides, T., and Obici, L. (2019). Patisiran, an RNAi therapeutic for the treatment of hereditary transthyretin-mediated amyloidosis. Neurodegener. Dis. Manag. *9*, 5–23. https://doi.org/10.2217/nmt-2018-0033.

81. Buya, A.B., Witika, B.A., Bapolisi, A.M., Mwila, C., Mukubwa, G.K., Memvanga, P.B., Makoni, P.A., and Nkanga, C.I. (2021). Application of lipid-based nanocarriers for antitubercular drug delivery: A review. Pharmaceutics *13*, 2041. https://doi.org/10.3390/pharmaceutics13122041.

82. Rosas-Taraco, A.G., Higgins, D.M., Sánchez-Campillo, J., Lee, E.J., Orme, I.M., and González-Juarrero, M. (2009). Intrapulmonary delivery of XCL1-targeting small interfering RNA in mice chronically infected with Mycobacterium tuberculosis. Am. J. Respir. Cell Mol. Biol. *41*, 136–145. https://doi.org/10.1165/rcmb.2008-0363OC.

83. Younes, N., Zhou, L., Amatullah, H., Mei, S.H.J., Herrero, R., Lorente, J.A., Stewart, D.J., Marsden, P., Liles, W.C., Hu, P., and Dos Santos, C.C. (2020). Mesenchymal stromal/stem cells modulate response to experimental sepsis-induced lung injury via regulation of miR-27a- 5p in recipient mice. Thorax *75*, 556–567. https://doi.org/10.1136/thoraxjnl-2019-213561.

84. Feuermann, Y., Kang, K., Gavrilova, O., Haetscher, N., Jang, S.J., Yoo, K.H., Jiang, C., Gonzalez, F.J., Robinson, G.W., and Hennighausen, L. (2013). MiR-193b and miR-365-1 are not required for the development and function of brown fat in the mouse. RNA Biol. *10*, 1807–1814. https://doi.org/10.4161/rna.27239.

85. du Sert, N.P., Hurst, V., Ahluwalia, A., Alam, S., Avey, M.T., Baker, M., Browne, W.J., Clark, A., Cuthill, I.C., Dirnagl, U., et al. (2020). The arrive guidelines 2.0: Updated guidelines for reporting animal research. Plos Biol. *18*, 1–12. https://doi.org/10.1371/journal.pbio.3000410.

86. Cottey, R., Rowe, C.A., and Bender, B.S. (2001). Influenza virus. Curr Protoc Immunol, 19.11.15–19.11.18.

87. REED, L.J., and MUENCH, H. (1938). A SIMPLE METHOD OF ESTIMATING FIFTY PER CENT. Am. J. Epidemiol. *27*, 493–497. https://doi.org/10.7723/antiochreview.72.3.0546.

88. Gupta, S., Lee, C.M., Wang, J.F., Parodo, J., Jia, S.H., Hu, J., and Marshall, J.C. (2018). Heat-shock protein-90 prolongs septic neutrophil survival by protecting c-Src kinase and caspase-8 from proteasomal degradation. J. Leukoc. Biol. *103*, 933–944. https://doi.org/10.1002/JLB.4A0816-354R.

YMTHE, Volume *31*

Supplemental Information

Preventing occludin tight-junction disruption via inhibition of microRNA-193b-5p attenuates viral load and influenza-induced lung injury

Chirag M. Vaswani, Amir K. Varkouhi, Sahil Gupta, Amin M. Ektesabi, James N. Tsoporis, Sadiya Yousef, Pamela J. Plant, Adriana L. da Silva, Yuchen Cen, Yi-Chieh Tseng, Sabrina S. Batah, Alexandre T. Fabro, Suzanne L. Advani, Andrew Advani, Howard Leong-Poi, John C. Marshall, Cristiana C. Garcia, Patricia R.M. Rocco, Guillermo M. Albaiceta, Steffen Sebastian-Bolz, Tania H. Watts, Theo J. Moraes, Vera L. Capelozzi, and Claudia.C. dos Santos

Figure S1.

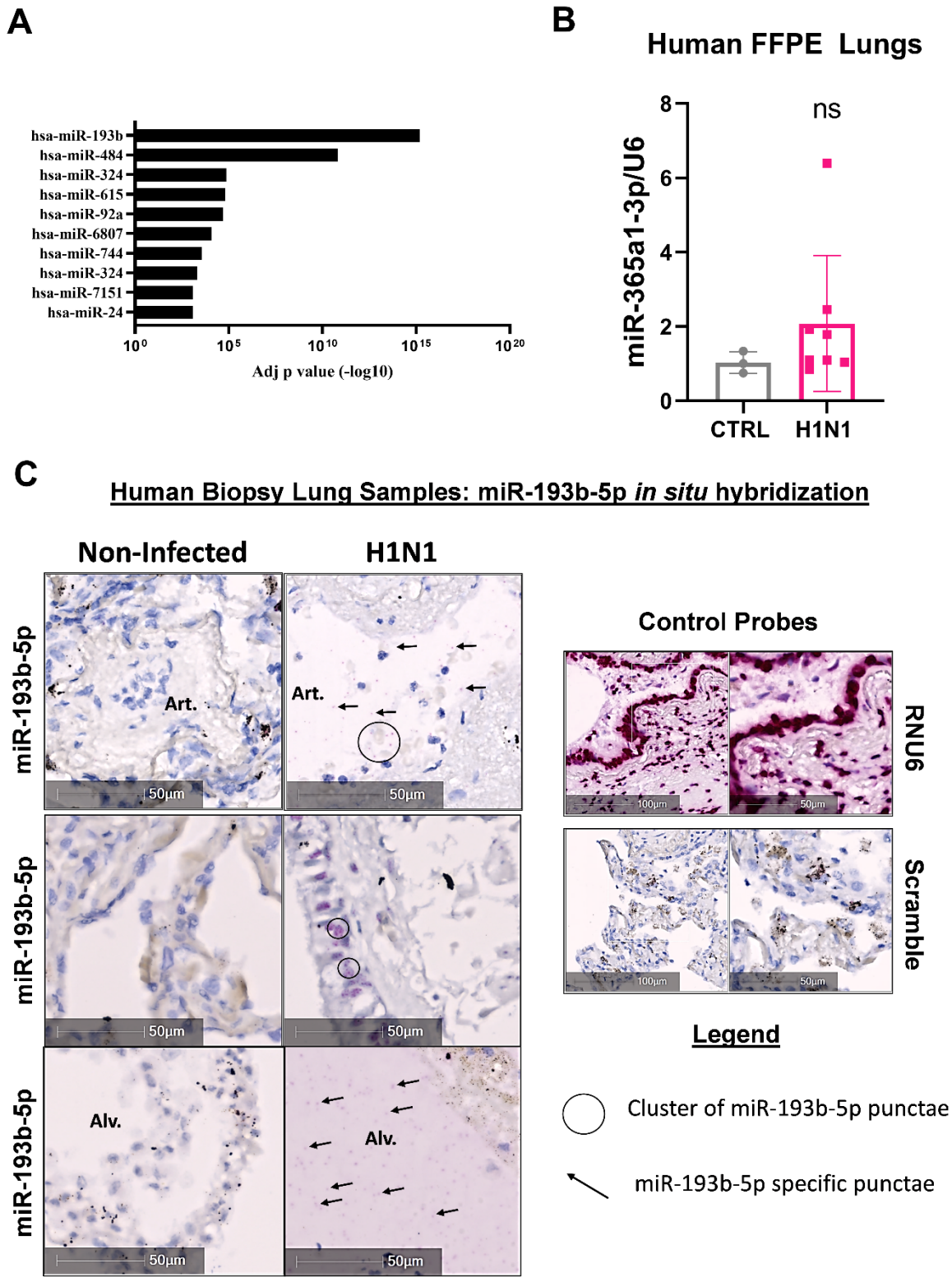
A
hsa-miR-193b
hsa-miR-484
hsa-miR-324
hsa-miR-615
hsa-miR-92a
hsa-miR-6807
hsa-miR-744
hsa-miR-324
hsa-miR-7151
hsa-miR-24
10^0
10^5
10^10
10^15
10^20
Adj p value (-log10)
B
Human FFPE Lungs
ns
miR-365a1-3p/U6
8
6
4
2
0
CTRL
H1N1
C
Human Biopsy Lung Samples: miR-193b-5p in situ hybridization
Non-Infected
H1N1
miR-193b-5p
miR-193b-5p
miR-193b-5p
Art.
Art.
Alv.
Alv.
50µm
Control Probes
RNU6
Scramble
100µm
Legend
Cluster of miR-193b-5p punctae
miR-193b-5p specific punctae

Figure S1. MiR193b-5p punctaes are spatially localized in human H1N1 lung bronchial epithelial, pulmonary artery and edema-filled alveolus space in situ.

A) Horizontal bar graph showing differential expression of miR-193b gene targets in human lungs from patients with H1N1 and non-infected controls. Transcriptomic data was analyzed for the top 3'UTR microRNA binding site enrichment among genes differentially expressed in influenza infected vs non infected lung obtained from consenting patients undergoing lobectomy. MiR-193b was the top predicted miRNA (adjusted p-value of 2.7e-11). **B)** MiR-365a1-3p is non significantly expressed in human infected H1N1 formalin fixed paraffin embedded tissues compared to non-infected. **C)** Representative photomicrograph of microRNAscope in situ hybridization of human lungs probed for miR-193b-5p showing that, compared to non-infected tissue, miR-193b-5p is localized in pulmonary arteries (Art), distal bronchi and edema filled alveoli (N=5). Cluster of miR-193b-5p punctae and specific punctae are indicated by circle and arrows respectively. Scrambled S1 probes for microRNAscope staining demonstrated the specificity of the miR-193b-5p in situ hybridization assay, and the highly expressed RNU6 demonstrates preservation of RNA in the mouse tissues.

Figure S2.

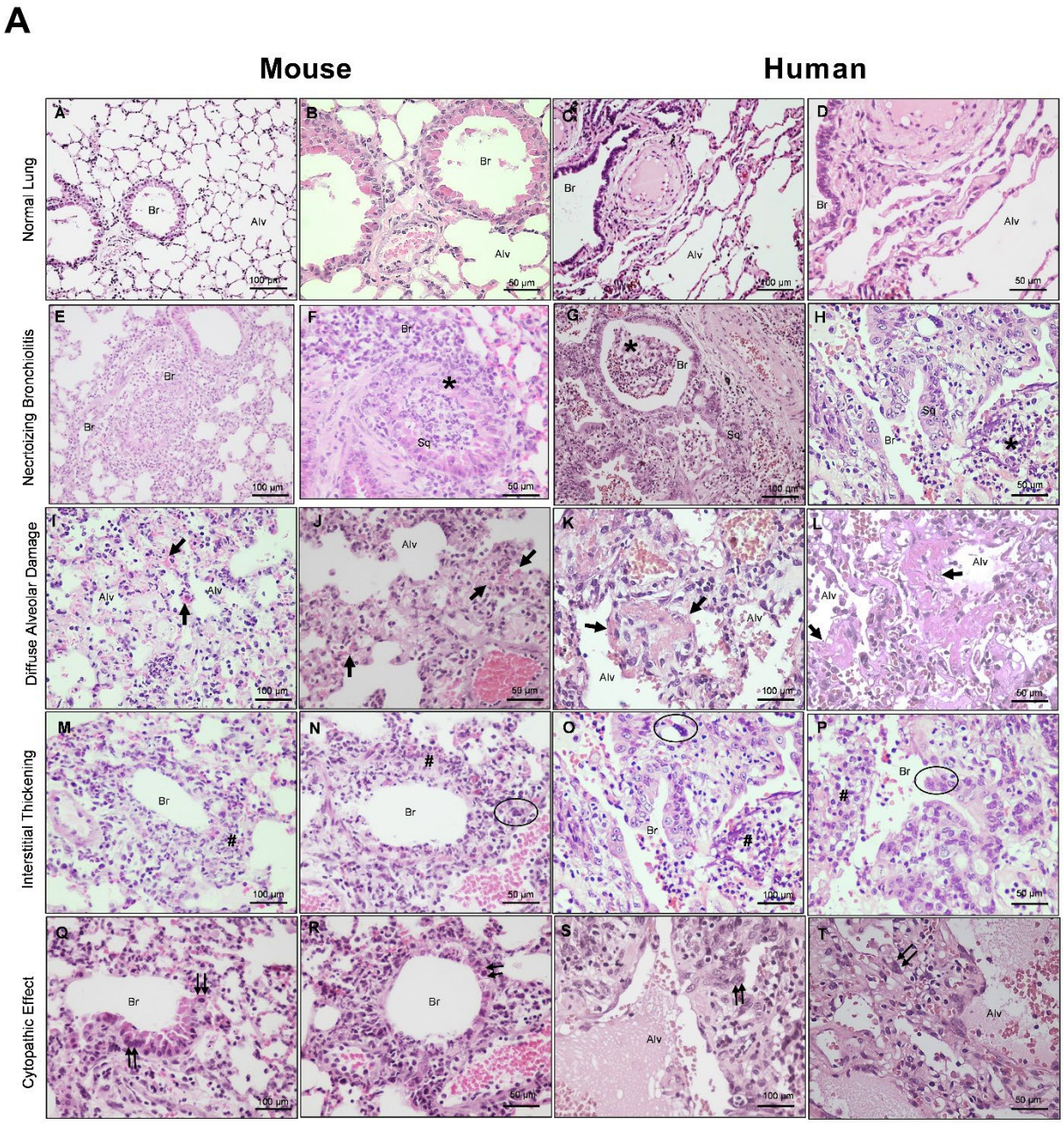
A
Mouse
Human
Normal Lung
Necrotizing Bronchiolitis
Diffuse Alveolar Damage
Interstitial Thickening
Cytopathic Effect
Br
Alv
Sq
100 µm
50 µm

Figure S2. Comparison between mouse and human histological features of severe PR8 induced lung injury vs human H1N1-induced ARDS.

A) Histoarchitecture of bronchiolar and alveolar parenchyma visualized at different magnification stained by Hematoxylin & Eosin. **(A_{A-D})** demonstrate normal histoarchitecture of bronchiolar and alveolar parenchyma, interstitial septa, and pulmonary arteries in mice and human non-infected controls. **(A_{E})** A low magnification showing the airway with centered inflammatory process and squamous metaplasia demarcated by mild inflammation on alveoli. **(A_{F})** A high magnification showing necrotizing bronchiolitis (*) with prominent epithelial necrosis with detachment of the basement membrane, interspersed with neutrophils exudate in the center and full thickness bronchiole by lymphocytes infiltration. A sub occlusion of the bronchiole was formed. **($A_{I,J}$)** Homogeneous septal thickening through inflammation and hyaline membranes (single arrows), and a prominent alveolar collapse, with intra-alveolar non-cardiogenic edema, characterizing a diffuse alveolar damage (DAD) histologic pattern. **($A_{M,N}$)** peribronchiolar septal interstitium homogeneously thickened by lymphocytes infiltration (#) with the maintenance of the alveolar histoarchitecture, consistent with an interstitial pneumonitis virus induced. **($A_{Q,R}$)** Bronchiolar epithelium (double arrows) and adjacent alveolar epithelium (N) showing cytopathic effect (circles). **($A_{E,F;G,H;}$)** Note the similarities between necrotizing bronchiolitis with squamous metaplasia (*) in H1N1 human and Influenza mice, **($A_{I,J;K,L}$)** diffuse alveolar damage (arrows), **($A_{M,N;O,P}$)** lymphocytic septal thickening with maintenance of the septal architecture (#), **($A_{S,T;\ Q,R}$)** in addition to viral cytopathic effect in bronchiolar epithelium (circles) and alveolar epithelium (double arrows) H&E, hematoxylin and eosin; Br, bronchiole; Alv, alveoli; Ar, artery; Sq, squamous metaplasia; Ed, edema.

Figure S3.

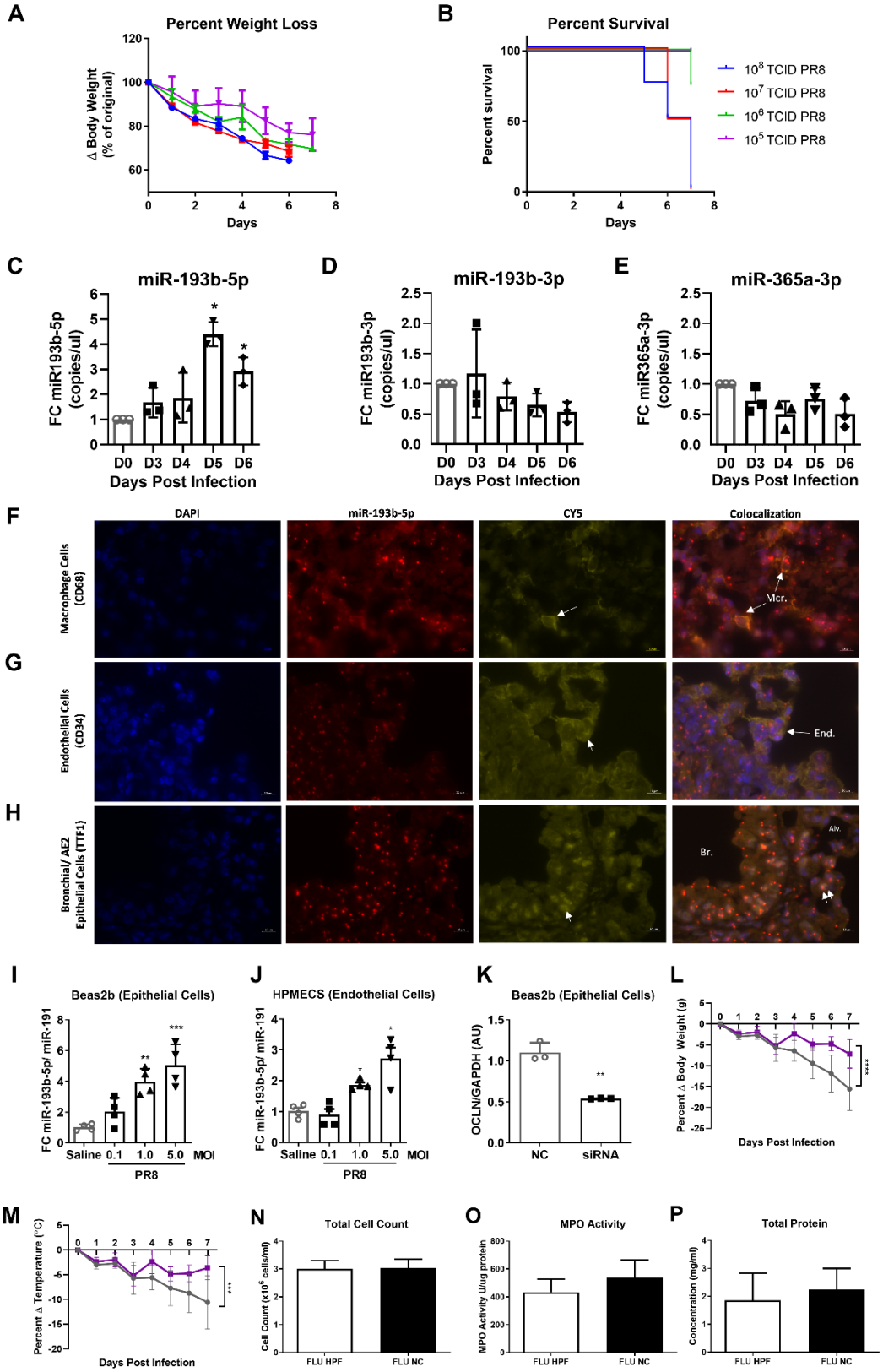
A
Percent Weight Loss
Δ Body Weight (% of original)
Days
B
Percent Survival
Percent survival
Days
10^8 TCID PR8
10^7 TCID PR8
10^6 TCID PR8
10^5 TCID PR8
C
miR-193b-5p
FC miR193b-5p (copies/ul)
D0 D3 D4 D5 D6
Days Post Infection
D
miR-193b-3p
FC miR193b-3p (copies/ul)
D0 D3 D4 D5 D6
Days Post Infection
E
miR-365a-3p
FC miR365a-3p (copies/ul)
D0 D3 D4 D5 D6
Days Post Infection
F
DAPI
miR-193b-5p
CY5
Colocalization
Macrophage Cells (CD68)
Mcr.
G
Endothelial Cells (CD34)
End.
H
Bronchial/ AE2 Epithelial Cells (TTF1)
Br.
Alv.
I
Beas2b (Epithelial Cells)
FC miR-193b-5p/ miR-191
Saline 0.1 1.0 5.0 MOI
PR8
J
HPMECS (Endothelial Cells)
FC miR-193b-5p/ miR-191
Saline 0.1 1.0 5.0 MOI
PR8
K
Beas2b (Epithelial Cells)
OCLN/GAPDH (AU)
NC
siRNA
L
Percent Δ Body Weight (g)
Days Post Infection
M
Percent Δ Temperature (°C)
Days Post Infection
N
Total Cell Count
Cell Count (x10^6 cells/ml)
FLU HPF
FLU NC
O
MPO Activity
MPO Activity U/ug protein
FLU HPF
FLU NC
P
Total Protein
Concentration (mg/ml)
FLU HPF
FLU NC

Figure S3. Viral titration in vitro and evaluation of microRNA-193b-5p response to increasing MOI for H1N1. Influenza A/Puerto Rico/8/34 infective dose titration in vivo and evaluation of microRNA-193b KO cluster by digital droplet (dd) PCR.

A) Body weight loss and **B)** percent survival in WT mice infected with increasing doses of Influenza A/Puerto Rico/8/34 (PR8). Data presented as means ± SEM (n = 4 per group). Digital droplet PCR (ddPCR) experiment demonstrating **C)** significant fold increase in detection of digital-droplets fluorescing miR-193b-5p Taqman probe, **D)** non-significant change in miR-193b-3p and **E)** miR-365a-1 expression. Each individual symbol in graphs represent results for an individual mouse in experiment. MicroRNAscope in situ hybridization of influenza infected mouse lung tissue with probe specific miR-193b-5p and its colocalization with **F)** lung macrophage (CD68) **G)** pulmonary endothelial (CD34) and **H)** epithelial (TTF1) cells (n=3-5). Abbreviations: Bronchial (Br), alveolus (Alv), Squamous Metaplasia (Sq), macrophage (Mcr), Endothelial (End). Increasing multiplicity of infection (MOI) of PR8 infected immortalized human bronchial epithelial cells (Beas2b) BEAS2b and human microvascular endothelial cells (HPMEC) shows **I)** significant increases in fold change of miR-193b-5p post PR8 infection in BEAS2b. **J)** HPMECS show significant increase in fold change of miR-193b-5p at 5 MOI post PR8 infection. **K)** Western blot densitometry shows reduced occludin protein expression in BEAS2b cells treated with siRNA-occludin. (n=4; *p<0.05, **p<0.01, ***p<0.001, Tukey's Multiple Comparisons Test, One-way Anova). MiR193bKO mice relative to WT exhibit significant improvement in physiological parameters including **L)** percent change in body weight (grams) and **M)** percent change in body temperature (ºC) by 7 dpi. Non-significant independent effect of HI Perfect (HPF) reagent compared to negative control (NC) from **N)** bronchoalveolar lavage fluid total cells count, **O)** Myeloperoxidase (MPO) and **P)** total protein count. (n=3-7, ***p<0.001, ****p<0.0001).

Figure S4.

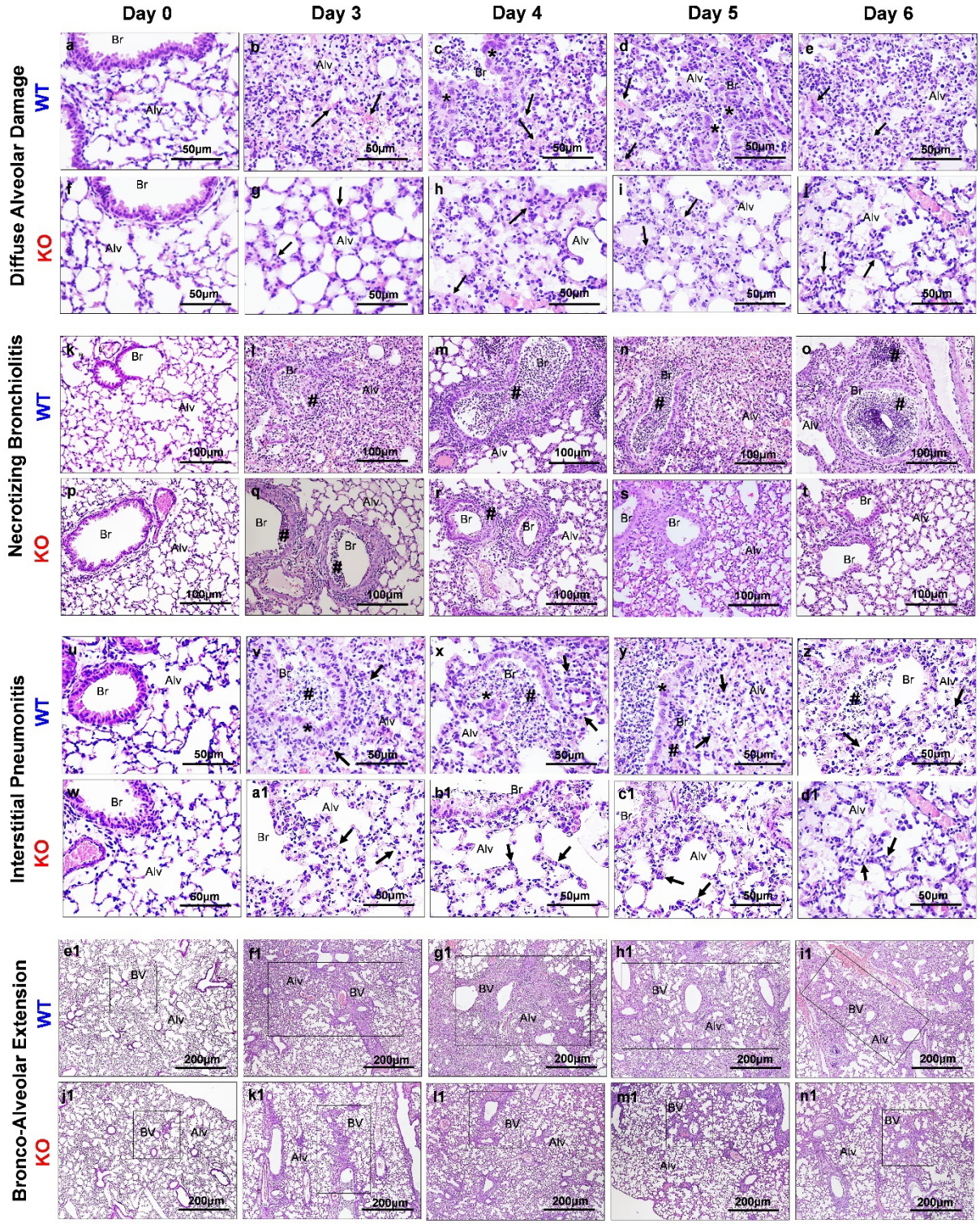
Day 0
Day 3
Day 4
Day 5
Day 6
Diffuse Alveolar Damage
Necrotizing Bronchiolitis
Interstitial Pneumonitis
Bronco-Alveolar Extension
WT
KO
Br
Alv
BV
50μm
100μm
200μm

Figure S4. miR193b KO infected with PR8 over time.

Lung morphology of H1N1 WT and miR193b KO animals after 0, 3, 4, 5 and 6- days visualized by hematoxylin & eosin-stained sections. At day 0, both groups present normal bronchovascular axis (Br), intact alveoli (Alv) and thin alveoli/capillary membranes (a-f; k-p; u-w; e1-j1; rectangles). At days 3 to 6 H1N1 WT animals show intense and progressive changes, being maximal the 4-days, characterized by diffuse distribution of the bronchovascular injury (rectangles, f1; g1; h1; i1), diffuse alveolar damage with hyaline membranes (long arrows, b; c; d; e), extensive necrotizing bronchiolitis (#; l; m; n; o) and interstitial pneumonitis (small arrows, v; x; y; z). Atypical bronchiolar (Bv*) and alveolar epithelial cells (Alv, *) were seen in all WT cases, although the distribution was focal. These atypical forms included multinucleated giant cells with irregularly distributed nuclei or bronchiolar and alveolar epithelial cells with large, atypical nuclei, prominent eosinophilic nucleoli, and granular amphophilic cytoplasm suggesting distinct viral inclusions. In contrast, at days 3 to 6 miR193b KO mice lungs exhibit animals less bronchovascular injury (rectangles, k1; l1; m1; n1), focal diffuse alveolar damage with hyaline membranes (long arrows, g; h; i; j), discrete necrotizing bronchiolitis (#; q; r) and interstitial pneumonitis (small arrows, a1; b1; c1; d1). Trained pathologists were blinded to the experimental groups assigned.

Figure S5. Primer sequences for miR-193-365-1 locus and representative gel.

Primer Pair 1	5'- GCG AAT GAG ACC AGA AGG AAA CTG -3'	5'- GGG CTC ATT GTG TCG CGT AAG G -3'
Primer Pair 2	5'- AGA AGA GTG ATG GCA TCT CTG ACG -3'	5'- GGG CTC ATT GTG TCG CGT AAG G -3'

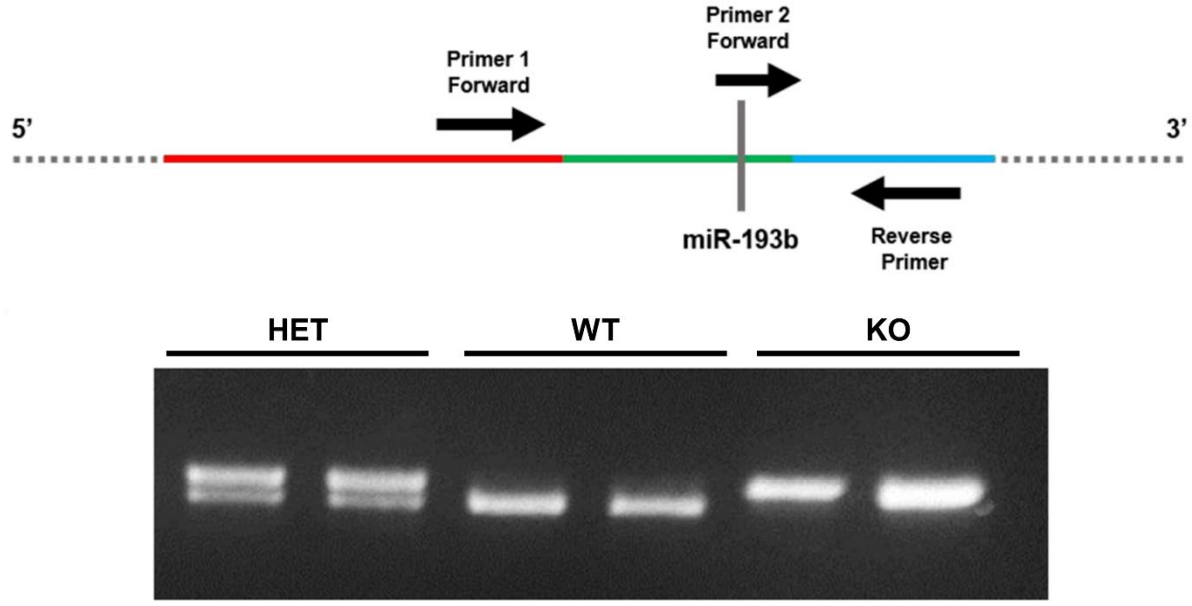

Table S1.

List of primers used in this paper.

MOUSE	Forward	Reverse
OCLN	5′ -CCAGCTCCAAGAAAGGACGA -3′	5′- CGCCCTGTAGGTGAGGTTAT-3′
MAVS	5’ ACA GCG CCA TCA AAA TTA CC-3’	5’ ATT TGG TCC AGT CTG GTT GC-3’
IFNß	5′ -CCAGCTCCAAGAAAGGACGA -3′	5′- CGCCCTGTAGGTGAGGTTAT-3′
IFITM1	5′-CCG AGA GAT GCC TAA GGA GCA GCA AGA GGTG-3′	5′-GCA AGA CAT CTC ACA TCA TCT AAT GGC-3′
IFITM3	5′-CCG CAC CAT GAA CCA CAC TTC TCA AGC C-3′	5′-CCT CTA TTA AGT GTG AAG GTT TTG AGC G-3’
IFNAR1	CACGGTCGCTGTAGAAGTAAAG	TCTCCTCCTCTTCGTTGGAATA
IL-6	5’-GAGGATACCACTCCCAACAGACC -3’	5’AAGTGCATCATCGTTGTTCATACA 3’
NOX-2	5’-ACT CCT TGG AGC ACT GG-3’	5’-GTT CCT GTC CAG TTG TCT TCG-3’
18S	5′-GCA ATT ATT CCC CAT GAA CG-3’	5′-GGC CTC ACT AAA CCA TCC AA -3′
36B4	5′-CAA CCC AGC TCT GGA GAA AC-3′	5′-GTT CTG AGC TGG CAC AGT GA-3′

HUMAN	Forward	Reverse
OCLN	5′ -CCAGCTCCAAGAAAGGACGA -3′	5′- CGCCCTGTAGGTGAGGTTAT-3′
MAVS	5` TCT TTT CAG GCA ACC ATT GC-3	5`ACT TGG AGC ATG GGA TGA AG 3`
IFNß	5`TCA GAG TGG AAA TCC TAA GG-3	5` CTG GTT GAA GAA TGC TTG AA 3`
IRF-1	5’-CAA ATC CCG GGG CTC ATC TGG-3’	5’-CTGGCTCCTTTTCCCCTGCTTTGT-3’
IFIT-1	5′ -TGCTCCAGACTATCCTTGACCT -3′	5′ -TCTCAGAGGAGCCTGGCTAA -3′
BST-2	5’-TGATCTCATCAGTTCTGAGCGGGT-3’	5’AGACCTGCTCCAGAGGCCCTTCTC3’
STAT1	5’- CGGCTGAATTTCGGCACCT -3’	5’- CAGTAACGATGAGAGGACCCT- 3’
18S	5’-GGCCCTGTAATTGGAATGAGTC-3’	5’-CCAAGATCCAACTACGAGCTT-3’

VIRUS	Forward	Reverse
PB1 (Influenza)	5’- GAG ACA CTG GCA AGG AGT ATA TG-3’	5’- GTC CAA GAT TCA GGA TGG AGA C- 3’
HA (Influenza)	5’- GGG TAT TCA TCA CCC GTC TAA C-3’	5’- CCG TAC CAT CCA TCT ATC ATT CC -3'
NA (Influenza)	5’ – CCC AAG GTG CCT TAC TGA AT- 3’	5’- ACA GCC ACT GCT CCA TTA TC- 3’